SANDIA REPORT
S A N D 2 0 0 6 - 6 7 5 4
Unlimited Release
Printed November 2006

Nanolithography Directed Materials Growth and Self-Assembly

Julia W. P. Hsu

Prepared by
Sandia National Laboratories
Albuquerque, New Mexico 87185 and Livermore, California 94550

Sandia is a multiprogram laboratory operated by Sandia Corporation,
a Lockheed Martin Company, for the United States Department of Energy's
National Nuclear Security Administration under Contract DE-AC04-94AL85000.

Issued by Sandia National Laboratories, operated for the United States Department of Energy by Sandia Corporation.

Available to DOE and DOE contractors from
U.S. Department of Energy
Office of Scientific and Technical Information
P.O. Box 62
Oak Ridge, TN 37831

Telephone: (865) 576-8401
Facsimile: (865) 576-5728
E-Mail: reports@adonis.osti.gov
Online ordering: http://www.osti.gov/bridge

Available to the public from
U.S. Department of Commerce
National Technical Information Service
5285 Port Royal Rd.
Springfield, VA 22161

Telephone: (800) 553-6847
Facsimile: (703) 605-6900
E-Mail: orders@ntis.fedworld.gov
Online order: http://www.ntis.gov/help/ordermethods.asp?loc=7-4-0#online

SAND200X-XXXX
Unlimited Release
P r i n t e d O c t o b e r 2 0 0 6

Nanolithography Directed Materials Growth and Self-Assembly

Julia W. P. Hsu
Surface & Interface Sciences
Sandia National Laboratories
P.O. Box 5800
Albuquerque, New Mexico 87185-MS1415

Abstract

We report a novel approach to assemble inorganic nanorystals: using micropatterned organic templates to manipulate surface nucleation energy for ZnO nanorods grown on silver substrates. Exquisite control in placement, selectivity, crystal orientation, and nucleation density was demonstrated. Complex, hierarchical nanostructures were created using organic growth modifiers, and could be placed at pre-determined sites by combining with the assembly approach. Simulation based on a model developed for selective area growth in metal organic chemical vapor deposition was performed to understand the effect of patterning in this solution based system. Furthermore, results from photoluminescence and cathodoluminescence studies indicate that the defects responsible for visible luminescence in this solution grown ZnO nanorods most likely reside in the bulk of the nanocrystals and are related to excess oxygen. In addition, we have developed a new method, solution stamping nanolithography (SSNL), to directly fabricate functional oxide and metallic patterns on flat and curved surfaces.

ACKNOWLEDGMENTS

I would like to thank my collaborators: Z. R. Tian (UAR), N. C. Simmons, C. M. Matzke, J. A. Voigt, J. Liu (PNNL), T. L. Sounart (Intel), E. D. Spoerke, Y. Jiang (UNM), M. E. Coltrin, D. A. Scrymgeour, D. R. Tallant, R. L. Simpson, N. A. Missert, R. G. Copeland, N. A. Chang, J. J. Richardson (UCSB), and P. G. Clem. In addition, we would like to thank R. G. Tissot and M. A. Rodriguez for X-ray characterization, D. L. Overmeyer for performing the YBCO crystallization, B. McKenzie for scanning electron microscopy support, K. Felmet and Y.-L. Loo for the resistivity stamps, J. Sigman for performing annealing experiment, E. Venturini for measuring the superconducting properties of the printed YBCO lines, Robert Kee and Huayang Zhu for advice on the infinite-series and numerical solutions of the growth models. Further more, we thank B. C. Bunker, A. Boal, D. L. Huber, C. Seager, J. Floro (UVA), P. Lu (NMIT) and J. Aizenberg for helpful discussions. This work is supported by the Sandia National Laboratories (SNL) Laboratory-Directed Research and Development Program (LDRD). SNL is a multi program laboratory operated by Sandia Corporation, a Lockheed Martin Company, for the Department of Energy under Contract DE-AC04-94AL85000.

CONTENTS

FIGURES

TABLES

NOMENCLATURE

DOE	Department of Energy
SNL	Sandia National Laboratories
μCP	microcontact printing
SEM	scanning electron microscopy
XRD	X-ray diffraction
HMT	hexamethylenetetramine
CBD	chemical bath deposition
SAMs	self-assembled monolayers
DAP	diaminopropane
TEM	transmission electron microscopy
HRTEM	high-resolution transmission electron micrscopy
EN	ethylene diamine
CTAC	hexadecyltrimethylammoniam chloride
SAG	selective area growth
MOCVD	metal organic chemical vapor deposition
PL	photoluminescence
PLE	photoluminescence excitation
CL	cathodoluminescence
CCD	charge couple device
PMT	photomultiplier tube
NBE	near-bandgap emission
SSNL	solution stamping nanolithography
CSD	chemical solution deposition
MIMIC	micromolding in capillaries
μTM	micro-transfer molding
DPN	dip pen nanolithography
PDMS	polydimethylsiloxane
nTP	nanotransfer printing

1. Directed Spatial Organization of Zinc Oxide Nanorods

The ability to precisely place nanomaterials at predetermined locations is necessary for realizing applications using these new materials. Using an organic template, we demonstrate directed growth of zinc oxide (ZnO) nanorods on silver films from aqueous solution. Spatial organization of ZnO nanorods in prescribed arbitrary patterns was achieved, with unprecedented control in selectivity, crystal orientation, and nucleation density. Surprisingly, we found that caboxylate endgroups of ω-alkanethiol molecules strongly inhibit ZnO nucleation. The mechanism for this observed selectivity is discussed.

1.1. Introduction

The ability to build nanostructured assemblies of technologically important materials requires both control of their placement ("patterning") and the structure and morphology of the materials themselves. A potentially powerful and economical approach to achieving the necessary control is nucleation and growth from solution. It is attractive to use patterned self-assembled monolayers (SAMs) as templates to direct inorganic crystal growth.[1,2,3,4] However, solution growth of technologically useful semiconductors based on this approach has yet been demonstrated. Here we report the success of using micropatterned SAM templates to direct the nucleation of zinc oxide (ZnO) nanorods following prescribed arbitrary patterns on a heterogeneous (silver) surface from an aqueous solution. The optical and electronic properties of a wide band gap semiconductor make the ZnO nanostructures promising for applications such as photovoltaics, active sensor platforms, and micro-lasers. We demonstrate a previously unattainable level of control in selectivity, crystal orientation, and nucleation density.

Recently there has been much research on the growth of arrays of ZnO columnar nanostructures by both catalytically activated vapor phase processes[5,6,7,8] and homogeneous precipitation in aqueous solutions.[9,10,11] To date, particularly with respect to growth in solution, techniques for simultaneously controlling both the patterning of the nanorods and the nanorod morphology have not been reported. We describe results in which patterning is achieved through formation of a ZnO "negative" of a microcontact printed SAM on a conducting substrate (Figure 1a). This is accomplished by inhibition of ZnO nucleation on the SAM through appropriate complexation of the SAM endgroup, while control of column size is obtained by use of growth modifiers.[12,13]

1.2. Experimental Session

The baseline process consisted of microcontact printing (μCP)[14] of 11-mercaptoundecanoic acid ($HSC_{10}H_{20}COOH$) SAM micropatterns on electron beam evaporated silver films. The chemically patterned Ag surfaces were then inserted into a dilute aqueous zinc nitrate ($Zn(NO_3)_2$) and hexamethylenetetramine (HMT; $(CH_2)_6N_4$) solution that was held at 50-60°C for several hours to nucleate and grow ZnO nanorods (Figure 1a). Microcontact printing creates a surface that is not homogeneous to ZnO nucleation: high barrier at SAM covered regions and low barrier at bare Ag regions. Consequently, the growth is selective and the spatial placement of ZnO nanorods is

dictated by the organic template. Examples of the high resolution of the process and its ability to precisely control ZnO nanorod placement are given in Figure 1b & 1c. Note that this is *not* a seeded growth;[11] ZnO nanorods grow directly on Ag. Figure 1b depicts the excellent selectivity achieved on such a SAM templated Ag surface: ZnO nanorods are found only inside the 1.4 μm width of the ring patterns and not on the surrounding SAM covered regions. Using this approach, we can routinely obtain spatial organization of ZnO nanorods over large areas (Figure 1c). Currently patterns over a ~ 1 cm x 1 cm area with good selectivity are achievable by performing μCP by hand in an ambient environment. The ability to create micropatterns of nanomaterials over large areas with good placement control is the first step in constructing devices using these materials.

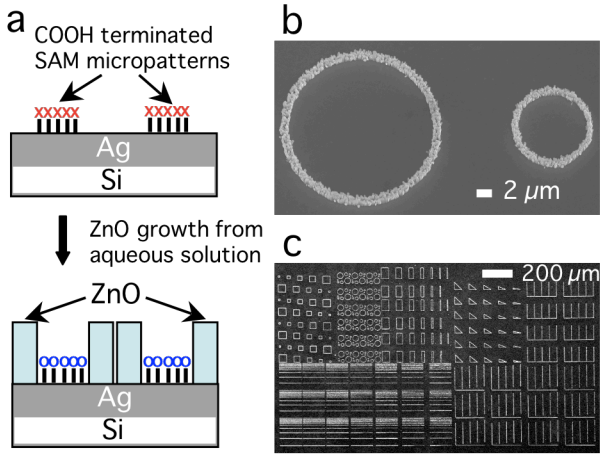

Figure 1. Organized ZnO nanorod growth on Ag directed by SAM patterns.
a, Schematics of μCP SAM patterns on Ag surfaces (top) and resulting positioning of ZnO nanorods nucleating on the bare Ag regions that were delineated by the organic template (bottom). x's in the top panel denote COOH endgroups of the SAM molecules, while o's in the bottom panel denote COO^-- HMT-H^+ complexes. b, Secondary electron microscope (SEM) images of ZnO nanorods organized in two rings. The surrounding regions are covered by $HSC_{10}H_{20}COOH$ SAM molecules, where no ZnO was found. c, Large-area patterns. ZnO nanorods appear white.

1.3. Results

Examples of the high resolution of the process and its ability to precisely control ZnO nanorod placement are given in Figure 1b & c. Note that this is *not* a seeded growth;[11] ZnO nanorods grow directly on Ag. Figure 1b depicts the excellent selectivity achieved on such a SAM templated Ag surface: ZnO nanorods are found only inside the 1.4 μm width of the ring patterns and not on the surrounding SAM covered regions. Using this approach, we can routinely obtain spatial organization of ZnO nanorods over large areas (Figure 1c). Currently patterns over a ~ 1 cm x 1 cm area with good selectivity are achievable by performing μCP by hand in an ambient environment. The ability to create micropatterns of nanomaterials over large areas with good placement control is the first step in constructing devices using these materials.

In addition to excellent spatial organization, ZnO nanorods grown by our method on Ag surfaces have the wurtzite structure (zincite) with a superb alignment of crystal orientation. This is seen in the scanning electron microscopy (SEM) image in Figure 2 inset and quantitatively examined using X-ray diffraction (XRD). The degree of crystal orientation is determined by comparing to XRD spectrum of randomly oriented powders (bottom panel of Figure 2), where the dominant peaks are (100) and (101). Enhanced (002) peak intensity indicates prevailing presence of ZnO crystals with c-axis ([001]) normal to surface. Previous reports of solution grown ZnO nanorods observed enhanced (002) peak over the more intense (100) and (101) peaks. However, all reflection peaks of ZnO were present in those works.[10,11] In contrast, only the (002) reflection is seen in our samples (top panel of Figure 2), even on the logarithmic scale. Therefore, ZnO nanorods are highly [001] oriented on Ag surfaces. This is further quantified by the full-width-half-maximum of the (002) rocking curve being ~ 5.8°. Our results represent a significant improvement in controlling crystal orientation over existing work.

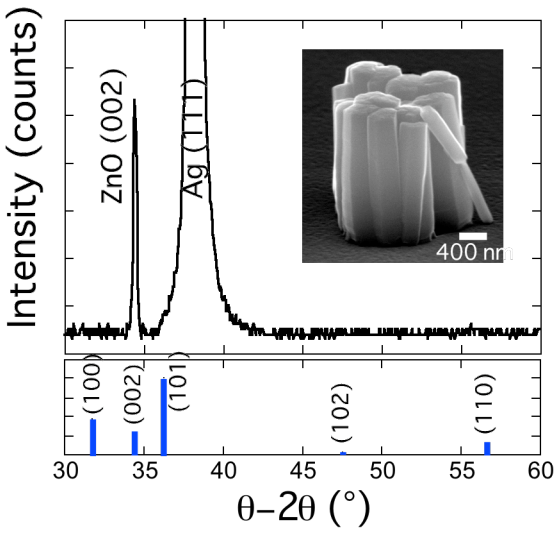

Figure 2. Highly oriented ZnO nanorods on Ag.
Top, X-ray diffraction $^{\theta}$-2θ scan of a patterned region showing only ZnO (002) and Ag (111) peaks. Inset, Side-view of ZnO nanorods in a 2-μm nucleation region showing strong c-axis textures. Bottom, Simulated $^{\theta}$-2θ scan of randomly oriented zincite powders showing the relatively intensity of each diffraction peak.

In addition to standard θ-2θ scans, pole figures were collected. The c- and a-axis lattice constants were measured to be 5.211(3) and 3.257(10) Å, respectively, consistent with values of 5.207 and 3.250 Å for zincite. While the mechanism behind the observed excellent crystal alignment is still under investigation, we note that the (111) plane of Ag has a hexagonal symmetry, the same as the basal plane of hexagonal ZnO. The difference between the a-axis lattice constant of ZnO and the nearest-neighbor lattice spacing of Ag in the (111) plane (2.892Å) is 11%, which might be sufficiently small for epitaxial growth.

Controlling nucleation density is another important aspect in spatial organization. In Figure 3, we show that nucleation density can be mediated through minute addition of a growth modifier,

sodium citrate.[12] Without sodium citrate, i.e. grown in solution containing zinc nitrate and HMT only, we found 46 ± 6 ZnO nanorods per 2-μm diameter nucleation region (Figure 3a). With the addition of 0.27mg/15 ml sodium citrate in the growth solution, one to two single crystals of ZnO platelets per 2-μm nucleation region have been achieved. Positioning individual single crystals of ZnO at precise, predetermined locations have not been achieved previously by either vapor or solution growth. Our result demonstrates that judicious choice of pattern size and solution chemistry offers control and flexibility in designing nanomaterials assembly.

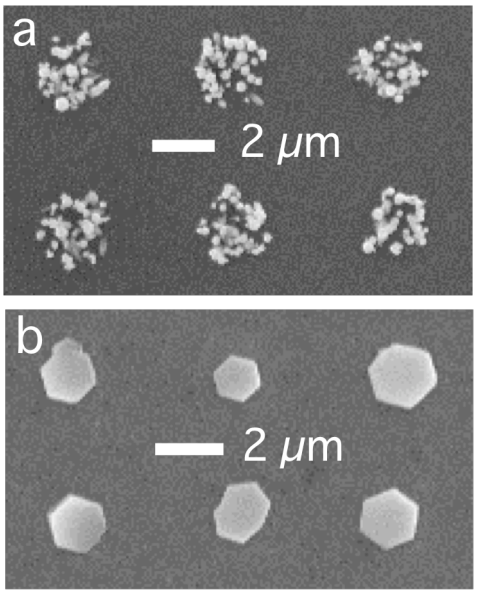

Figure 3. Effect of growth modifier on nucleation density.
Contrast between nanorods grown in (a) solution containing zinc nitrate and HMT only (46 ± 6 crystals per 2-μm diameter nucleation site) and (b) platelets grown in solution with 0.27mg/15ml sodium citrate (1 – 2 crystals 2-μm diameter nucleation site).

1.4. Discussions

The mechanism behind the nucleation selectivity in our system is puzzling because several inorganic crystals have been reported to grow on COOH terminated SAMs.[1,4,15,16] To better understand the selective nucleation in our system, we first consider the solution chemistry of the process. The initial pH of the $Zn(NO_3)_2$/HMT solution is 6.7 and remains relatively constant throughout the nucleation and growth processes. For this pH and the zinc concentration used (0.02M), the predicted dominant zinc species present will be hydrated Zn^{+2}, along with a much smaller amount of $ZnOH^+$.[17] Also, in this pH range an amine in the HMT will be rapidly protonated to form the $(CH_2)_6N_4$-H^+ complex.[18] With prolonged heating, a closed aqueous HMT solution continues to consume protons, ultimately going to a liquid-vapor equilibrium in which the solution will contain partially decomposed HMT complexes, ammonia (NH_3), and formaldehyde (CH_2O) with the vapor containing a mixture of H_2O, NH_3, and CH_2O.[19] For the system used in this work, the hydroxyl byproduct of the continuous uptake of protons by the HMT provides a controlled, continuous source of OH^- required for the hydrolysis and precipitation of ZnO.

The interaction between charged species in the solution and surface functional groups governs heterogeneous nucleation on surface. At pH of 6.7, the COOH endgroups of the SAM are de-protonated and are negatively charged.[20] The positively charged Zn growth species and HMT-H^+ complexes can compete for binding with the carboxylate endgroups of the SAM. To explore this interaction, we performed an experiment that exposed the SAM patterned Ag to different chemicals prior to growth. Figure 4a shows a ZnO sample grown by first immersing a SAM patterned Ag film for 5 minutes in an aqueous solution containing only $Zn(NO_3)_2$; no HMT. As seen in Figure 4a, ZnO has nucleated and grown on the SAM. In contrast, ZnO nucleation and growth occurs only on bare Ag regions (Figure 4b) with no Zn^{+2} pre-treatment. Without the presence of SAM, ZnO nanorods nucleate and grow on Ag uniformly at a relatively low nucleation density, as shown in Figure 4c. The results of this experiment qualitatively agree with a picture in which the HMT-H^+ preferentially complexes with the carboxylate endgroups of the SAM, creating an effective electrostatic and/or steric block that inhibits ZnO nucleation on the SAM. When the carboxylate-terminated SAM was allowed to complex with Zn^{+2} first, the SAM surface become energetically favorable for ZnO nucleation, producing results similar to what has been reported in other works.[2,4,15,16] The nucleation is less controlled with Zn^{+2} pre-treatment; this may be due to exchange of the Zn species with the HMT-H^+ complex when HMT is introduced. In general, heterogeneous nucleation on surface was found to be sensitive to the SAM preparation and the pre-treatment procedures.

A striking consequence of inhibiting ZnO nucleation at the SAM covered regions is the effect of patterning on nucleation density. The nucleation density when confined in 1.4-μm width (~ 12/μm^2, Figure 1b) is much greater than that of a unpatterned bare Ag film (~ 1.0/μm^2, Figure 4c). We postulate that shutting off nucleation at SAM regions results in the supersaturation conditions generated near the film/solution interface to be relieved through increased ZnO nuclei density in the nearby uncoated Ag regions.[2]

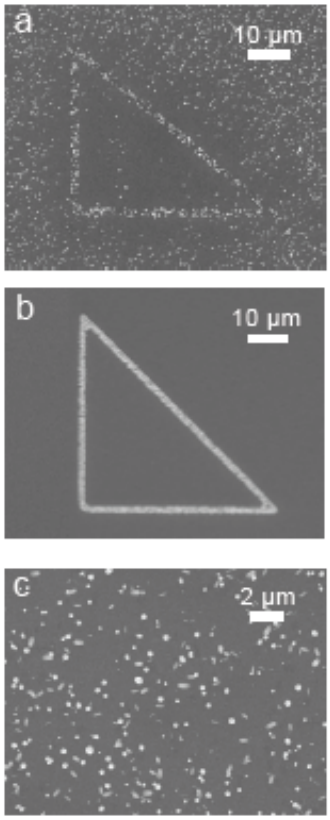

Figure 4. Role of HMT in surface nucleation.
a, The SAM patterned Ag surface was first exposed to $Zn(NO_3)_2$ only for 5 minutes before HMT was added. ZnO nucleation on the SAM regions as well as bare Ag was observed in this case. b, Normal growth with SAM patterned Ag surface exposed to $Zn(NO_3)_2$ and HMT mixture simultaneously. Inhibited nucleation of ZnO on SAM regions was found. c. ZnO growth on a bare Ag surface, i.e., not covered by SAM.

1.5. Summary

In this paper, we report the successful application of using patterned organic templates to direct ZnO nanorod growth on silver surface. We show unprecedented control over selectivity, nucleation density, crystal orientation, and spatial organization of ZnO nanorods over large areas following prescribed arbitrary patterns. These results demonstrate the viability using organic templates to direct the growth of technologically useful inorganic nanocrystals from solutions.

2. SEQUENTIAL NUCLEATION AND GROWTH OF COMPLEX NANOSTRUCTURED FILMS

Nanostructured films with controlled architectures are desirable for many applications in optics, electronics, biology, medicine, and energy/chemical conversions. Low-temperature, aqueous chemical routes have been widely investigated for the synthesis of continuous films, and arrays of oriented nanorods and nanotubes. More recently, aqueous-phase routes have been used to produce films composed of more complex crystal structures. In this paper, we discuss recent progress in the synthesis of complex nanostructures through sequential nucleation and growth processes. We first review the use of multi-stage, seeded growth methods to synthesize a wide range of nanostructures, including oriented nanowires, nanotubes and nanoneedles, as well as laminated films, columns, and multilayer heterostructures. We then describe more recent work on the application of sequential nucleation and growth to the systematic assembly of large arrays of hierarchical, complex, oriented, and ordered crystal architectures. The multi-stage aqueous chemical route is shown to be applicable to several technologically important materials, and therefore may play a key role in advancing complex nanomaterials into applications.

2.1 Growth of Oriented Nanocrystalline Films

Nanostructured films and coatings with controlled surface area, porosity, crystalline orientation, grain sizes, and crystal morphologies are desirable for many applications, including microelectronic devices, chemical and biological sensing and diagnosis, energy conversion and storage (photovoltaic cells, batteries and capacitors, and hydrogen storage devices), light emitting displays, catalysis, drug delivery, separation, and optical storage. Meeting the demands of these potential applications, however, will require reliable and economic processes for the production of a large supply of high quality nanomaterials. Gas-phase reactions[21] have been extensively used to prepare oriented nanostructures including carbon nanotubes,[22,23] ZnO nanowires,[24,25] and many other oxide and non-oxide semiconductor materials,[26,27] but these methods typically require high temperatures (~500–1100 C) and vacuum conditions, which limit the choice of substrates and the economic viability of high-volume production. These limitations have stimulated research on solution-phase synthesis (sometimes referred to as the soft solution route or chemical bath deposition (CBD)), which offers the potential for low-cost, industrial-scale manufacturing. Low-temperature (typically < 100 C), aqueous-phase approaches are particularly attractive because of their low energy requirements, and safe and environmentally benign processing conditions.

In aqueous-phase synthesis, oriented nanocrystalline films are deposited on a substrate in aqueous media by heterogeneous nucleation and subsequent growth. The resultant film structure is controlled by a complicated set of coupled processes in both the solution and solid phases. Heterogeneous nucleation on the substrate is promoted over homogeneous precipitation in solution by controlling the precursor supersaturation levels and the interfacial energy between the substrate and the new phase to be formed.[1] Two basic approaches have been used to nucleate films: direct deposition and deposition on chemically modified interfaces using organic self-assembled monolayers (SAMs).[28] Without surface modification, the free energy of crystallization on the native substrate interface must be intrinsically low enough to relieve the supersaturation

and induce direct film growth. This affects the choice of substrates and film structure for a particular solution chemistry. SAMs containing surface-active groups have been shown to promote heterogeneous nucleation by reducing the free energy of formation of the crystalline phase.[1,29,2] The functional molecules in the SAMs can be chosen to control the nucleation density and the crystalline phase and orientation. Nucleation and growth of calcium carbonate on SAMs has been extensively studied[29] because of its relevancy to biomineralization[30] and many nanostructured ceramic films, including vertically oriented iron oxide or hydroxy-oxide nanorods on SAMs have also been reported.[31,32]

Recently, several researchers have discovered aqueous chemistries and substrates that support direct deposition of oriented nanocrystalline films. Vayssieres et al.[33,34] reported the growth of large oriented arrays of akaganeite (β-FeOOH) nanorods directly on tin oxide or alumina, with the akaganeite being converted to hematite (α-Fe_2O_3) or ferromagnetic iron nanorods via subsequent treatment. This approach was extended to ZnO by thermally decomposing metheneamine in the presence of $Zn(NO_3)_2$ to produce large arrays of oriented ZnO rods, about one to two μm in diameter.[10] Longer reaction times led to preferred dissolution of the ZnO rods on the metastable (0001) polar surfaces, and produced hollow hexagonal microtubes.[35] Arrays of much smaller ZnO nanorods were later obtained by reducing the $Zn(NO_3)_2$ concentration.[36] The conditions for synthesizing ZnO nanorod arrays from aqueous solutions were recently reviewed by Govender et al.,[37] and similar aqueous chemical routes have been developed to grow oriented arrays of nanorods and nanotubes of other metal chalcogenides and hydroxides.[38,39,40,41,42] Electrochemical deposition in aqueous solutions has also been applied to directly deposit oriented films of ZnO nanorods,[43,44,45,46,47,48] cuprous oxide nanocubes, nanopyramids,[49] and several other crystal habits.[50]

To date, most of these solution-synthesis methods have produced either continuous film structures or arrays of nanorods or nanotubes. Although a few studies have recently reported tower-, tube-, and flower-like morphologies resulting from the addition of organic growth modifiers,[51,52,53] fabrication of more complex nanostructures, such as those observed in natural materials or biominerals,[54] remains a significant challenge. In this article, we discuss multi-stage synthesis strategies for systematically adding complexity to oriented nanocrystals. This approach has provided an opportunity for rational design and synthesis of controlled architectures in nanostructured films.

2.2. Seeded Crystal Growth

Multi-step synthesis of complex nanostructured films often begins with substrate surface preparation for heterogeneous nucleation of oriented nanocrystals. On many substrates, this can be accomplished with SAMs, but an even more straightforward approach is to seed the substrate with nanoparticles of the desired film material. We and other groups developed seeded growth methods that permit control over the size, population density, and spatial distribution of the crystals. Several classes of materials, such as ZnO, TiO_2, CdS, and polymers have been studied. Nanoparticles are often widely available through commercial sources or can be readily prepared using techniques reported in the literature. The seeds can be deposited on the substrate using many mature techniques, such as dip/spin coating,[11,12,55,56,57,58] sol-gel coating,[59,60] or electrophoretic deposition.[61] In most seeding techniques, the nanoparticles are produced in a

separate process before physical deposition on the substrate. However, atomic layer deposition,[62] RF magnetron sputtering,[63,64,65] solution coating,55 hydrothermal pretreatment,[66] and electrochemical deposition[67,68,69] produce a nanoparticle seed layer during an initial deposition step. Once the seed layer is formed, oriented nanocrystal growth follows in a second step. These two-step processes hint at the potential of using multiple reaction steps to control nanostructured film synthesis.

When nanoparticles are applied as the seeds, nanocrystal orientation and alignment is accomplished through competition.[12] Since the nuclei (or the seeds) are generally not well aligned on the substrate, the new crystal growth from these seeds will have no preferred orientation initially. However, as the crystals, such as nanorods, grow along the favored crystal planes, those that are not aligned normal to the substrate are soon impeded by neighboring crystals, and do not have room for further growth. Only the crystals with the growth orientation normal to the substrate can continue to grow, thus forming the oriented arrays. The size and population density of the seeds on the substrate primarily determines the size and population density of the oriented nanocrystals.

ZnO nanorod arrays of highly uniform orientation have been produced from epitaxial growth on <0001> oriented seed layers.[55,59] In this case, there is no competitive growth, and the nanorod orientation is dictated by the seed orientation. Oriented seed layers have been prepared by repeatedly coating glass or silicon substrates with solutions of zinc acetate in ethanol or zinc acetate/methanolamine in methoxyethanol, followed by heat treatment at 350 – 800 C. Although the fundamental mechanisms are not clear, the heat treatment produces vertically aligned nanocrystals that function as the seeds for large arrays of vertical ZnO nanowires.

The fundamental advantage of seeded growth is the enhanced control imparted by separating nanoparticle film nucleation and oriented rod growth into two steps. In each step, different experimental conditions can be used to optimize and control each one independently. Extending this concept, we have used several synthesis steps to produce oriented nanostructures that are much more complex than simple nanorod architectures (Figure 5). In this methodology, the materials produced in one step function as the substrate for the next step. The desired nanostructures are produced by altering the experimental conditions in a controlled fashion between the different steps. For example, after seeding a glass substrate (Figure 5a), ZnO crystals are grown along the <0001> orientations to form long prismatic nanorod arrays (Figure 5b). In subsequent steps, organic molecules are added to change the surface chemistry so that the initial rods will grow into different shapes (Figure 5c and d). Adding citrate, for example, reduces the aspect ratio of the rods. During ZnO nanorod growth, citrate preferentially adsorbs to the (0001) surfaces, which inhibits crystal growth along the [0001] direction and produces fatter and shorter crystals.[12] By controlling various additive concentrations, and the number of growth steps, we have systematically controlled the aspect ratio of the nanorods, changed the crystal morphology from rods (Figure 5e) to needles (Figure 5f) to tubes (Figure 5g) to stacked columns (Figure 5h) and to plates (Figure 5i), grown isolated nanorods or oriented dense films (Figure 5j), and produced even more complicated bilayer structures.[12] Hirano et al. has also reported an aqueous multi-step process to prepare oriented ZnO microcrystals similar in structure to Figure 5j.[70] While some of the other morphologies have also been reported using single step synthesis, such as solution grown micro/nanotubes[35,64] and gas-phase derived nanotubes and

nanoneedles,[22,23,71] a key advantage afforded by the aqueous, multi-stage approach is the ability to systematically generate and control a diverse array of structures from an otherwise similar and inexpensive chemical route.

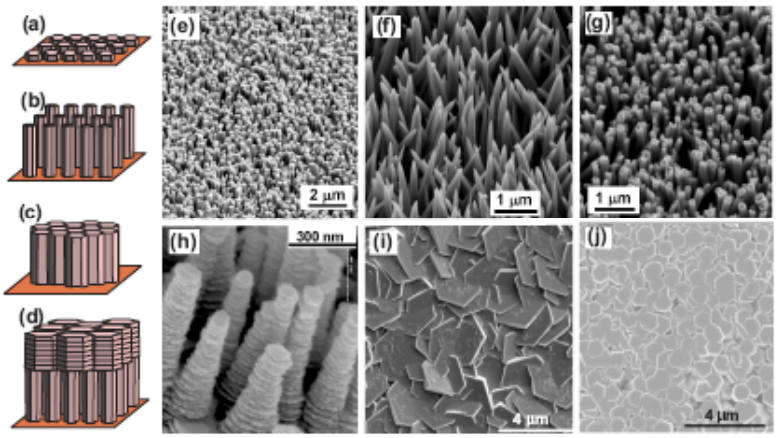

Figure 5. One-step and multi-step seeded growth of large arrays of oriented nanostructured ZnO films from aqueous solution synthesis.
Schematic illustration in (a)-(d) and SEM images of example array structures in (e)-(j): a) nucleation seeds on a substrate; b) oriented nanorods from seeded growth; c) densely populated ZnO rod array from secondary growth; d) two-layer structure with one layer of nanorods and another layer of nanoplates, from multi-step growth. e) nanorods; f) nanoneedles; g) nanotubes; h) stacked columns; i) nanoplates formed on nanorods; j) dense arrays of large, oriented ZnO crystals. (e) to (i) were synthesized on glass microscope slides after seeding with ZnO nanoparticles; the arrays in (e)-(g) required one seeding step and one growth step, and those in (h)-(i) involved multiple growth steps after seeding.

The multi-step, seeded growth technique is applicable to materials other than ZnO. For example, oriented conductive polymer nanowires have been produced by a multi-stage electropolymerization and electrochemical deposition process.[67,68] In the first step of the process, a high current density is applied to yield a dense and uniform array of polymer nanoparticles on the substrate. In subsequent steps, the current density is sequentially reduced to suppress the creation of new polymer particles and promote polymerized growth from the existing polymer seeds. Other nanocrystalline films produced with two-step, seeded growth include oriented arrays of $CaCO_3$ nanowires[69] and TiO_2-based nanotubes.[56] The oriented arrays of TiO_2-based nanotubes are grown using TiO_2 nanoparticle seeds dipcoated on Ti foil.

2.3. Hierarchical Crystal Growth

Two-step, seeded growth of simple one dimensional oriented nanocrystalline films and multi-stage growth of more complicated nanostructures are vanguards for a process to systematically assemble complex, hierarchical crystal architectures. In the previous section, we discussed multi-stage aqueous reactions that have been used to tune the morphology of oriented crystalline films by altering the crystal growth behavior in each stage, but without nucleating new branched crystals after the first stage. Several groups have recently used more than one synthesis step to nucleate new oriented nanocrystals on crystals formed in a previous reaction step. In gas-phase

synthesis, Dick et al.[72] first synthesized GaP and InP semiconductor nanowires, and then sequentially reseeded the nanowire surfaces to produce tree-like nanostructures. In solution-phase synthesis, similar ZnO[73] and ZnO/TiO_2-based[74] composite nanostructures were produced by multi-step precipitation of powders in bulk aqueous solutions. We have investigated multi-step, aqueous nucleation and growth methods that have produced higher-order, hierarchical films of several important minerals. In the hierarchical growth method, the first step is to create nucleation sites, via processes such as seed deposition or micropatterning of SAMs (Figure 6). Oriented nanocrystals grow from these nucleation sites, and in subsequent reaction steps, new crystals nucleate and grow on the crystals produced in previous stages. This provides the capability to build a diverse range of complex nanostructures from various primary subunits that can be tuned by the growth chemistry in each step.

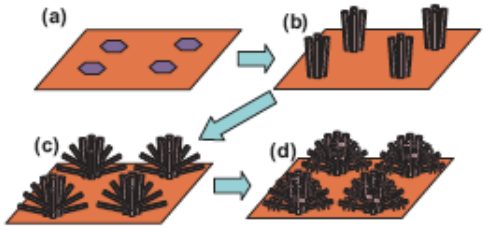

Figure 6. Schematic illustration of the multi-step, sequential nucleation and growth method leading to truly hierarchical structures.
a) creation of nucleation centers on a substrate by, e.g., micropatterning or microstamping; b) growth of patterned nanorods on a substrate; c) secondary growth from the patterned nanorods; d) tertiary growth from the secondary rods.

2.4. Renucleation and Growth on ZnO

Higher-order ZnO crystal structures assembled from rod- or needle-shaped primary subunits have been synthesized with a sequential nucleation and growth process. In one approach, primary ZnO rods are first prepared on a clean glass substrate (Figure 7a). During the second step, new crystals grow on the surfaces of the primary rods when bifunctional diaminoalkane molecules are added to the solution (Figure 7b). The structure observed in Figure 7b is similar to the rotor-like crystals observed in homogeneously nucleated powders,[73] but further crystal growth produces extended secondary crystals of star-like or comb-like morphology when viewed parallel or normal to the primary crystal c-axis, respectively (Figure 7c). In the third step, the tapered secondary crystals are "healed" to the hexagonal prismatic shape, and in the fourth step, additional branch crystals nucleate from the secondary structures to form unusual wagon wheel-like crystals (Figure 7d). Therefore, with multiple reaction steps, new nucleation sites and a variety of large supercrystal structures can be created (Figure 7e-f). Morphological variations between the structures, such as the size, population density, and shape of the rods in each stage, can be precisely controlled with the solution chemistry in each step.

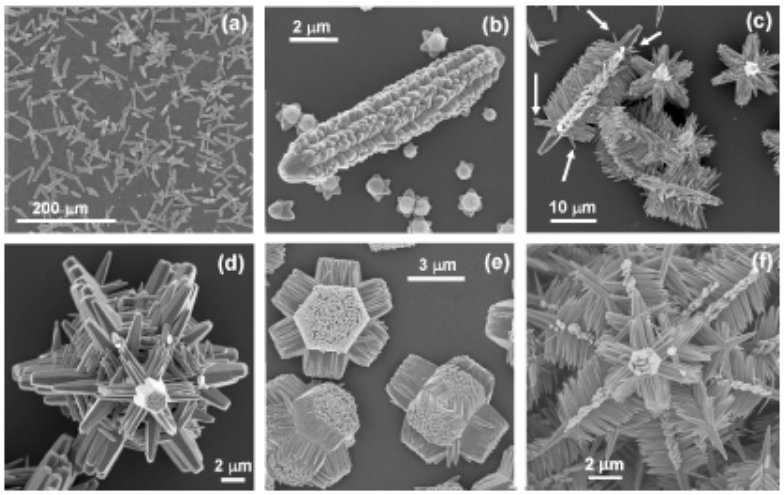

Figure 7. . Hierarchical ZnO crystals formed by multi-step growth (SEM images). a) primary ZnO crystals—bicrystals with the middle (0001) surface and the two flat $(000\bar{1})$ terminal surfaces; b) secondary crystals nucleated from the primary crystals; c) 2nd-order crystal structure with long secondary crystal branches; d) tertiary crystal from renucleation on the secondary crystals in (c); e) dense arrays of secondary structures; f) tertiary crystal with long needles from three growth stages, using diaminobutane (DAB) to nucleate branch crystals. The secondary crystal in (b) is observed at an early stage of growth (1 hr), and the crystals in (c)-(f) have had time (at least 6 hrs in final growth step) to mature to equilibrium conditions.

The creation of new nucleation events that produce secondary crystal growth is a critical step for the success of the multi-stage approach. Without the diamine molecules, new nucleation is not observed after the primary stage, and repeated crystal growth simply increases the primary crystal size. SEM, TEM, and HRTEM studies have elucidated the details of the renucleation process in the presence of diaminopropane (DAP). An initial layer of polycrystalline nanoparticle seeds (bright dots in the dark-field image) nucleate without well defined morphology or alignment (Figure 8a-c). The dark-field TEM image (Figure 8c), shows the polycrystalline nature of the nuclei and their misalignment with respect to the parent crystal and themselves. The possible role of diamine molecules in creating new nucleation sites on ZnO surfaces was discussed by Gao et al.,[53] who suggested that ethylene diamine (EN) adsorbs to the high energy sites on ZnO and reduces the surface energy, thus promoting heterogeneous nucleation. The adsorption of diamine molecules on ZnO prismatic surfaces is well documented,[52,75] and we further speculate that the diamine molecules may be bifunctional, viz. that one of the terminal amine groups binds to the existing ZnO crystal surface, and the other terminal group binds to the solution species (Zn^{2+}, $Zn(OH)^{+}$, etc.[76]), either through electrostatic interaction or complexing.[52,75] This may induce the attachment of reactive species on the surface and cause nucleation to occur rather than epitaxially enlarge the crystals.

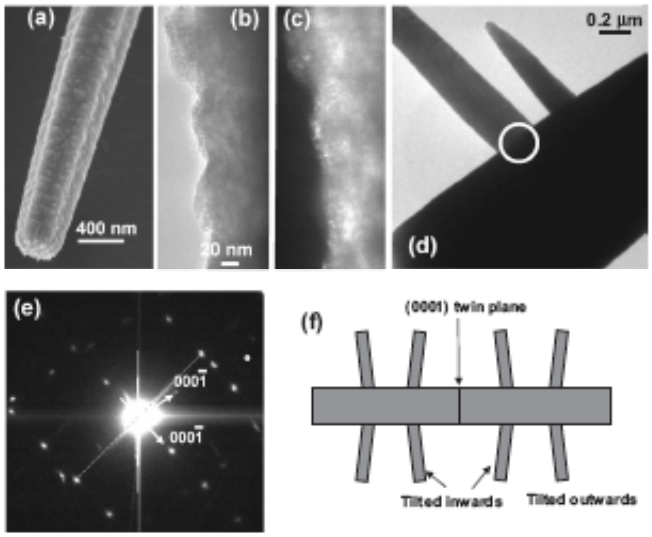

Figure 8. Secondary nucleation on primary ZnO crystals.
a) polycrystalline coating of ZnO nuclei on primary ZnO crystal surface (SEM); b) bright-field TEM image of the nuclei; c) dark-field TEM image of the nuclei, showing polycrystalline nature (in dark-field TEM imaging, only diffracted light from one crystal plane is collected); d) bright-field TEM image of the interface between branched and parent crystals; e) selected-area diffraction from the interfacial region circled in (d), showing rotation and superimposition of two possibly twin-related patterns; f) schematic illustration of $(1\bar{1}02)$ type twins showing two possible tilting angles. The primary ZnO crystals were grown on clean glass, and the secondary reaction was suspended after 30 minutes of incubation for (a)-(c), and 6 hours for (d) and (e).

As the secondary branch crystals grow from the polycrystalline film, the [001] orientation is normally tilted about 80 ± 3° with respect to that of the parent crystals (Figure 8d), and normally bends toward the center (Figure 7c). This orientational relationship between the two crystals is also revealed in the selected area diffraction pattern at the interface (Figure 8e), which shows two superimposed electron diffraction patterns (wurtzite structure, a = 3.2495 Å and c = 5.2069 Å). Solution syntheses of ZnO produce either bipyramidal twinned crystals that are bisected by the $(000\bar{1})$ twinning plane, or dumbbell-shaped bicrystals that are bisected by a central (0001) twinning plane.[77] In our synthesis, we exclusively observe the dumbbell-shaped twinned crystals with a flat terminal surface. The polarity is thus pointed away from the terminal surface, towards the central (0001) twinning plane. The orientation of the secondary crystals that is observed experimentally in SEM images and in the superimposed diffraction pattern could be reproduced by a twining operation about a $(1\bar{1}02)$ plane. In ZnO, the calculated angle between the c axes of the two crystals with this twinning relationship is 85.6°, which is in reasonably good agreement with the experimental values results. However, exactly how the new crystals are related to the parent crystals as they nucleate and grow, and the nature of the interface between the crystals have not been well studied at this time. It is also possible that the particular angle observed is due to some other growth behavior, such as coincident lattice matching. Work is being done to reveal the origin of the unusual crystal growth behavior.

Figure 8f shows the two possible orientations of the secondary crystals viewed from the $[11\bar{2}0]$ zone axis, assuming that they are twin related. The branch crystals could then either tilt away from or towards the central (0001) plane. Experimentally, both configurations are observed, but the crystals tilting towards the middle plane are much more common (Figure 7c). This difference may be caused by the lack of inversion symmetry and spontaneous dipole along the c axis of ZnO crystals. The preferential selection of the tilting direction could be the result of minimizing interfacial energy during the nucleation of the secondary crystals, similar to what was suggested in Ref. 78. However, as indicated by the arrows in Figure 7c, sometimes (particularly near the edge of the crystals or close to a substrate surface) branch crystals are pointed outwards.

Most of the ZnO crystals observed in Figure 7 have a conical, tapered or needle-like shape due to the presence of diamine molecules. In the literature, diamine molecules are reported to play several roles.[52,75] They can adsorb to the prismatic surfaces, either through complexing with metal ions or through electrostatic attractions, and they can also complex with metal ions in solution and thus increase mineral solubility. We have observed that conical-shaped (tapered) nanorods, and nanoneedles are only produced with the addition of diaminoalkanes. Growth without such diamine molecules always produces straight prismatic rods in our experiments. Secondary growth of the conical rods without the diamine actually restores the regular prismatic shape. The mechanism by which diamines direct the formation of conical rods or needles is not clear, but preferential adsorption of the diamine molecules on the prismatic surfaces may play a role; the conical surfaces are made of numerous tiny {0001} steps, and during crystal growth, the diamine molecules may adsorb onto the prismatic surfaces and help preserve these steps.

2.5. Micropatterning of Hierarchical ZnO Films

Two-dimensional patterns of oriented nanocrystals can be created by modifying the spatial distribution of the interfacial energy on a substrate. For example, Aizenberg et al.[2,79,80] investigated the combination of SAMs and soft lithography (microstamping or microcontact printing) to prepare spatially controlled micropatterns of calcite crystals on a surface with precisely controlled location, nucleation density, size, orientation, and morphology. Mineral nucleation was favored on acid-terminated regions, but suppressed in methyl-terminated regions where the influx of nutrients was maintained below saturation. We applied similar microcontact printing techniques to grow oriented ZnO nanorods on patterned substrates.[81] Extended microarrays of carboxyl-terminated alkylthiols were printed on electron beam evaporated silver films. When the patterned silver substrates were placed in aqueous zinc nitrate solutions, oriented ZnO nanorods formed on the bare silver surface, but not on the surface covered by the carboxylic acid groups (Figure 9a). Using this approach, we were able to make patterned lines, dots, and a variety of structures, and control the density and the spacing to micron scales (Figure 9). In most lines and dots, multiple nanorods were observed because the nanorods were significantly smaller than the patterns (inset in Figure 9d). However, single crystal patterning has been obtained by growing the crystals to larger than 1 μm in size (inset in Figure 9b).

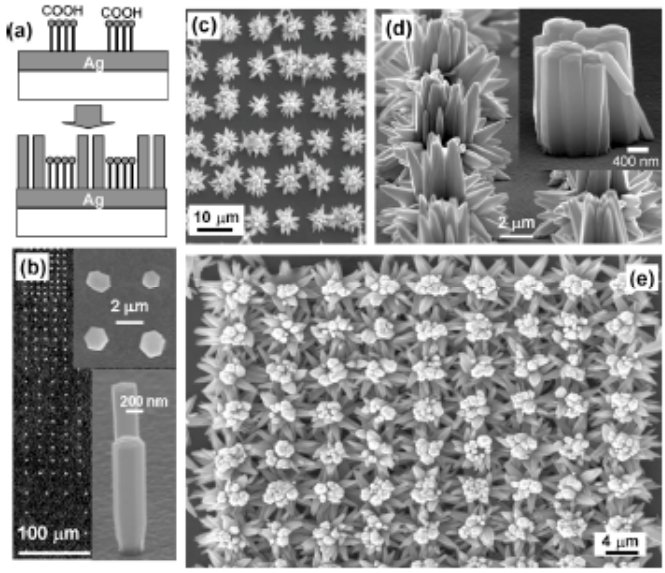

Figure 9. Micropattering of hierarchical ZnO crystals.
a) schematic illustration of micropattern chemistry for patterned ZnO growth; b) dotted patterns of vertically oriented nanorods and patterned single crystals (inset); c) micropatterned arrays of separated, secondary flower-like structures; d) side-view of micropatterened array in (c) with the inset showing the first generation seed bundles; e) dense micropatterned array of secondary ZnO "flowers". The patterned nanorod arrays and single crystals in (b) were synthesized on Ag substrates in one growth step after microstamping, and the flower-like crystals in (c) and (d) were grown in a second stage on patterned arrays like that shown in (b)-bottom inset. (b)-(e) are SEM images.

We produced micropatterns of hierarchical ZnO nanorod clusters by diamine-induced sequential nucleation and growth on micropatterned primary crystals, such as those shown in Figure 9b. Secondary growth produced flower-like crystals from new crystal growth on the top face of the primary rods and side branches formed on the edge. Figure 9c,d show arrays of ordered flower-like ZnO structures that formed during secondary growth on a micropattern of oriented primary rods with the top and side view, and Figure 9e show a densely packed arrays of similar structures in which the secondary crystals are almost connected. The variation in the orientation of the side branches arises in part from variations in the orientation of the primary rods in each bundle (Figure 9d inset), and in part from the effect of substrate on the relative orientation between the primary and secondary crystals. Oriented ZnO nanorods grown on silver substrates normally retain only half of the bicrystals with (0001) face at the silver interface (Figure 9b, bottom inset). The normal orientation of the secondary crystals observed for bicrystals (Figure 7 and Figure 8) would suggest that the secondary side-branch crystals should bend towards the substrate. However, the presence of the substrate physically hinders growth in that direction, and so many branches are tilted away from the substrate, towards the solution. Star-like or flower-like ZnO has been observed by several groups,[52,53,75] and it has been suggested that such ZnO crystals form through $(11\bar{2}2)$ twinning, with sheets lying between spines (needles).[82] In our studies, however, $(11\bar{2}2)$ twinning is not observed.

Additional growth steps with DAP produce a pattern of tertiary structures with fine-branched crystals, such as those shown in Figure 10. Some of these small tertiary subunits also nucleate sparsely on the substrate off the pattern, but it is remarkable how well the substrate is protected by only a monolayer through four reaction stages conducted over the course of several days. The length, morphology, and population density of the tertiary subunits are tunable with the reaction conditions as discussed previously. Thus, by combining top-down micropatterning techniques with bottom-up chemical synthesis control, complex tertiary "cactus-like" crystals can be tuned in structure and organized spatially on a substrate.

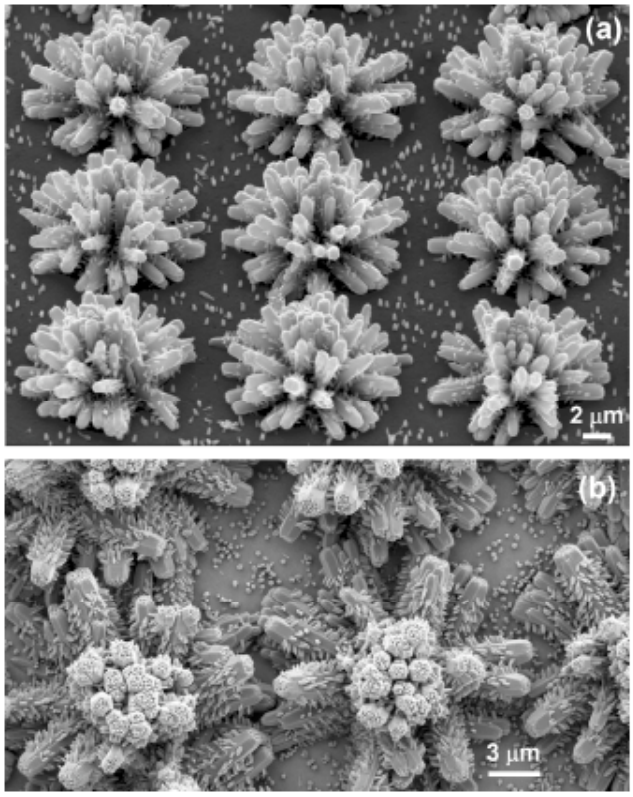

Figure 10. Micropatterned array of tertiary ZnO "cactus" structures (SEM images), produced with four growth stages on a microstamped Ag substrate.
a) micropatterned array viewed at an oblique angle; b) dense array viewed normal to the substrate.

2.6. Wide Applicability

The assembly of hierarchical nanocrystals by repeated nucleation and growth is not limited to synthesis of ZnO crystals. We previously demonstrated a novel hierarchical and self-similar crystal growth process leading to spontaneous formation of large mesophase silicate objects (several microns) in the presence of hexadecyltrimethylammoniam chloride (CTAC) surfactant with controlled morphology and ordering from nano- to macro-scale.[83] We first created well-defined and oriented mesophase silicate crystals on a glass surface. Transmission electron microscopy (TEM) showed that these mesophase crystals have a cubic structure. The crystals are octahedral (Figure 11a,b), truncated by the (111) surface, and are oriented with one of the {111}

planes parallel to the substrate. Hierarchically ordered crystals were assembled (Figure 11a) by multistage growth; in each step, new crystals were nucleated on the existing crystals, as is the case with ZnO. Figure 11c shows the secondary structure viewed from different angles, indicating that these crystals are made of the primary octahedral subunits like those in Figure 11b. The secondary structure is about 11 μm in width—two times the size of the primary structure—and is based on a quartet-octahedron model with 24 edge-sharing octahedral primary subunits. The model contains four surfaces made of six subunits and six corners made of four subunits. Figure 11d shows tertiary structures, and the inset shows how the new crystals nucleated on the edge of the existing crystals; higher-order structures can be derived by continued edge-sharing growth (Figure 11e). These large mesophase crystals are remarkable in several ways. First, these structures are not close-packed and contain large empty spaces, but they still have almost perfect octahedral shapes. Second, the octahedral subunits in the large structure are all about 5 μm in size and are fairly uniform. These subunits are also well aligned throughout the crystal by edge-sharing. Finally, the high-order octahedral mesophase crystals are also uniform in size.

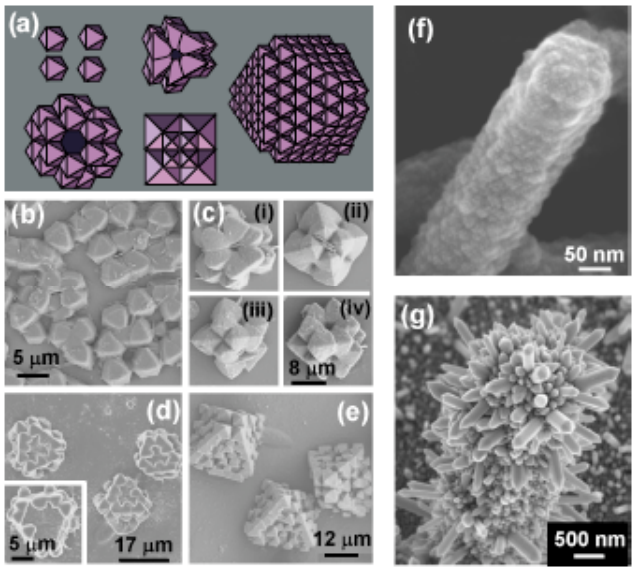

Figure 11. Higher-order structures beyond ZnO.
a) schematic illustration of assembling higher-order structures by nucleating new crystals through edge sharing configuration; b) octahedral primary crystals formed from the cubic self-assembled silicate; c) secondary structures formed from 24 primary crystals and viewed from different angles; d) tertiary structures; the nuclei on the secondary structure are visible in the inset; e) higher-order structures; f) ZnO nanorod coated with CdS nanoparticle seeds; g) CdS nanorods on ZnO crystal. CdS nanorods in (g) were grown on ZnO rods after pretreatment with CdS seeds as in (f), requiring three growth stages. (b-g) are SEM images. (a-e) reproduced from ref 83 with permission from *Angew. Chem. Int. Ed.*

One of the important extensions of stepwise materials assembly is its application to mixed material systems. We have recently demonstrated stepwise assembly of hierarchical heterostructures by growing cadmium sulfide (CdS) nanorods on ZnO crystals (Figure 11f, g). This process involves first nucleating and growing ZnO hexagonal rods, as described above. In a

second step, CdS nanoseeds are nucleated on the ZnO crystal surfaces from a solution containing cadmium nitrate and thioacetamide as a sulfur source. This process relies on the gradual release of free sulfide ions from thioacetamide during gentle heating, which prevents massive homogeneous nucleation of CdS, and allows for heterogeneous nucleation of CdS on ZnO rods (Figure 11f). In the third growth step, this CdS layer serves both to protect the ZnO and to seed the growth of CdS rods in a harsh reaction solution containing cadmium nitrate, thiourea and EN at elevated temperature and pressure. This multi-step process effectively produces nanorods of CdS radiating outwards from ZnO rod substructures (Figure 11g). Though the mechanisms for CdS rod formation have not yet been elucidated, the evolution of this rod morphology is attributed to the influence of EN, much like the secondary rod growth described for ZnO is tied to the presence of diamines. This example of mixed material assembly demonstrates the wider applicability of the multi-stage growth process and reiterates the importance of organic growth modifiers, such as diamines, in controlling selective stages of assembly.

2.7. Concluding Remarks

While important discoveries continue to be made in nanomaterials research, the field is advancing towards the development of applications. Oriented nanocrystalline semiconductor films are receiving increasing attention because of their powerful optical and electronic properties. High quality crystallinity, orientational alignment, and high surface/volume ratios are all important for efficient electron and photon transport in applications such as photovoltaics and lasers. With ZnO, large nanorod arrays of exceptional uniformity, orientational alignment, and optical properties (negligible defect emission) have been produced by the aqueous solution route. Room-temperature UV lasing has also been demonstrated, and water-repellent superhydrophobic surfaces with contact angles greater than 160 ° have been synthesized from ZnO nanorod arrays grown in aqueous solution.

Most of the progress towards applications has been with ZnO because of the established morphological control and because it is a multifunctional material of great engineering significance. However, as discussed in the current review, research on materials such $CaCO_3$ and SiO_2 inspired many of the developments that have led to the progress with ZnO, which may in turn inspire further progress with other materials. Research on other nanostructured film materials, such as TiO_2, Cu_2O, and CdS, is in a nascent stage, and synthesis of complex nanostructures has just begun.

This progress notwithstanding, the potential for nanostructured films still remains largely untapped. Fulfilling this potential will require greater control of film properties, informed by a better understanding of nanocrystal nucleation and growth phenomena. Developments in solution-phase synthesis have been mostly empirically derived, and mechanisms offered in the literature have been qualitative, speculative, and incomplete. Extensive and systematic studies are needed to elucidate the principles governing the control of the observed crystalline morphologies. The fundamental mechanisms controlling renucleation and growth on existing crystals are also not well understood, and it is not clear how single crystal formation and epitaxial alignment is achieved from polycrystalline renucleation layers. Furthermore, the factors that control the surface chemistry and the crystal morphologies and sizes cannot be systematically predicted. These scientific questions will need to be addressed in future studies in

order to gain the control and reliability required by nanomaterials applications. With this improved understanding and concomitant control, stepwise solution-phase growth methods should provide versatile and powerful industrial-scale production processes for assembling complex nanostructured films by design, and may ultimately be instrumental in moving nanoscience out of the laboratory and into technology.

3. MASS-TRANSPORT AND KINETIC EFFECTS IN SOLUTION-BASED SELECTIVE-AREA GROWTH OF ZnO NANORODS

We present a quantitative study of the dependence of ZnO selective-area growth on pattern dimension. Selective growth is achieved by patterning a portion of the substrate with an organic template that inhibits growth. The density of ZnO nanorods increases as the distance between the exposed growth regions is made greater. By systematically varying the dimensions of the exposed and masked regions, the experiments showed that growth was partially controlled by a length scale associated with diffusive mass transport within the reactant solution. A 2-D model was developed which describes the selective growth at the exposed surface regions, the competing loss of reactant material due to parasitic chemistry in the solution bulk, and diffusive mass transport to the growth surface. The simple model provides a good qualitative and semi-quantitative explanation of the experimental observations.

3.1. Introduction

Zinc oxide (ZnO) nanostructures have many potential applications due to their optical and electronic properties. ZnO is a direct band-gap semiconductor (Eg=3.37 eV) making it attractive for near UV optoelectronic uses, such as chemical / biological sensors, blue or UV light emission, and solar energy conversion. Its large exciton binding energy (60 meV) makes ZnO nanostructures interesting for high-temperature, high-power electronics applications. The lack of a center of symmetry in its wurtzite structure gives rise to large piezoelectric and pyroelectric effects, which would allow fabrication of unique nano-mechanical sensors or actuators from ZnO nanostructures.

ZnO nanostructures are often synthesized by vapor processes, such as thermal evaporation from a solid zinc oxide source, metal-organic chemical vapor deposition (MOCVD), or by a vapor-liquid-solid (VLS) technique employing a metal catalyst. There is much current work to control the synthesis and properties (such as size, placement, and alignment) of ZnO nanostructures.

Solution-based methods are attractive for low-temperature, economical, and environmentally benign growth of ZnO nanostructures. We are using organic molecules that form self-assembled monolayers (SAMs) to direct placement of ZnO nanorods grown from solution. Soft lithograph techniques are used to apply growth template patterns which control the spatial placement and, as shall be discussed, thenanorod density and growth rate[84]. Use of micro patterned SAM templates to direct growth of ZnO nanorods can produce remarkable control in growth selectivity, crystal-growth orientation, and nucleation density.[81,84] Nanorod nucleation density and growth rate was shown to depend on the pattern dimension,[81] suggesting that chemical reaction time scales or transport effects are important in this system.

In order to achieve better quantitative control and manipulation of the growth process we have developed a theoretical model of the selective-area solution-based growth of ZnO nanorods. The goal of the modeling is identify the rate-controlling phenomena of the crystal growth, e.g.,

chemistry or mass-transport effects. Specially designed growth mask patterns are used for comparison with model predictions and to identify physical parameters in the calculations.

The following section describes the experiment growth procedures and data analysis for nanorod density and size distribution. After that, the model formulation and method of solution are presented. Predictions of the model and a discussion of the competing affects of growth kinetics and mass transport are given in the next section of the paper. An analysis of ZnO nanorod growth in our experiments is given in terms of model predictions, and the paper concludes with a short summary section.

3.2. Patterned Growth of ZnO Nanorods

The ZnO nanorods were grown from aqueous solutions of 20 mM zinc nitrate and 20 mM hexamethylenetetramine at 60^{o}C for 3 hours. Substrates consisted of electron-beam deposited Ag films (thickness 1000Å) on Si wafers. An organic template was formed on the Ag substrate by using microcontact printing (μCP) of 16-hexadecanethiol (Aldrich, used as received) with 12 different patterns. ZnO nanorods were found to selectively grow on the bare Ag regions, i.e., areas not covered by the organic molecules, with the <0001> axis preferentially oriented perpendicular to the Ag substrate. Details of patterning and growth can be found in Ref. 81.

A total of 12 patterns of differing dimensions were used for the growth experiments. Each pattern consisted of repeated lines (4 mm long) with exposed windows of width w of bare Ag (upon which ZnO nucleation and growth can occur) separated by masked lines of width m covered by the organic molecules (where no growth occurs). The 12 patterns (referred to by their dimensions in μm as w:m) were: 1:1, 1:2, 1:4, 1:8, 1:16, 1:32, 2:4, 2:16, 4:4, 4:16, 8:4, and 8:16.

Scanning electron microscope (SEM) images were acquired using a LEO 1430 with 25 kV beam voltage. The areal coverage of the ZnO nanorods for each pattern was obtained from SEM images using ImageJ software. At least 10 lines were analyzed for each pattern. The height distributions of the nanorods were measured from at least 10 individual ZnO nanorods for each pattern using an atomic force microscope (Dimension 3100) operating in tapping model.

3.3. Model Description

The nanorod growth experiment can be treated as a transient, 2-D problem. The exposed lines for the selective nanorod growth are so long (4 mm) compared to pattern dimensions (on the order of 10's of μm's) that the third dimension can be neglected. The model assumes a uniform concentration of reactant in solution at time $t=0$, at which growth begins. Growth can occur at the lower boundary, i.e., the substrate, governed by a rate constant k_s. Destruction of the reactant species from crystal growth sets up a concentration gradient, giving rise to diffusive mass transport from the bulk solution toward the surface. We allow for the possibility of an unwanted (parasitic) loss of reactant due to formation of ZnO within the bulk solution[1] via a first-order rate constant k_b; this process competes with the desired nanorod growth at the surface. The process proceeds in time until the reactant species are depleted (through nanorod growth or from the parasitic loss).

This section begins with analysis of blanket, i.e., unpatterned, growth for this system (Section 3.1). When there is no lateral patterning the system is one-dimensional. It is instructive for identifying the dimensionless variables that govern the system, and because an exact solution exists. This initial analysis is extended to 2-D in Section 3.2.

3.3.1. Blanket Growth

3.3.1.1. Governing Equations

The model for blanket growth is shown schematically in Figure 12. As mentioned above, there is only one physical dimension, perpendicular to the growth direction. The quiescent solution containing an initial concentration C_i of reactant species has a height $y=y_m$. Growth begins at time $t=0$, setting up a time-dependent reaction / diffusion problem. The time-rate-of-change of reactant concentration at every point in the domain (bulk of the solution) is given by

$$\frac{\partial C}{\partial t} = D\frac{\partial^2 C}{\partial y^2} - k_b C\,, \tag{1}$$

where D is the reactant's diffusion constant. The boundary condition at the surface ($y=0$) ensures that the flux of reactants at the lower surface J_{y-} equals the rate of destruction due to growth,

$$J_{y-} = D\frac{\partial C}{\partial y} = k_s C\,. \tag{2}$$

A zero-flux boundary condition is imposed at the top of the domain $y=y_m$,

$$J_{y+} = D\frac{\partial C}{\partial y} = 0\,. \tag{3}$$

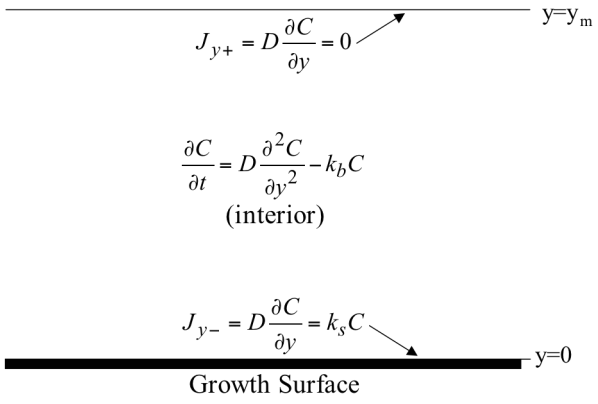

Figure 12. Schematic diagram for the 1-D model for unpatterned growth.

3.3.1.2. Dimensionless Equations

It is instructive to consider the non-dimensional form of the equations just introduced. Dimensional analysis is a means to simplify a problem by identifying the smallest number of unique (dimensionless) parameters needed to describe the system. For example, two different

physical systems that share the same set of dimensionless parameters are said to be *similar* and yield redundant results.

Define the dimensionless length scale and dimensionless concentration as

$$\hat{y} \equiv \frac{y}{y_m};\ \hat{C} \equiv \frac{C}{C_i}. \tag{4}$$

Further, define the dimensionless time as

$$\hat{t} \equiv \frac{tD}{y_m^2}. \tag{5}$$

Substituting these definitions, it is easy to verify from equation (1) that the dimensionless species continuity equation is

$$\frac{\partial \hat{C}}{\partial \hat{t}} = \frac{\partial^2 \hat{C}}{\partial \hat{y}^2} - Da_b \hat{C}, \tag{6}$$

where Da_b is the dimensionless Damköhler number for the bulk (solution) phase

$$Da_b \equiv \frac{k_b y_m^2}{D}. \tag{7}$$

The lower and upper boundary conditions (2) and (3) become the dimensionless conditions

$$\frac{\partial \hat{C}}{\partial \hat{y}} = Da_s \hat{C} \tag{8}$$

$$\frac{\partial \hat{C}}{\partial \hat{y}} = 0, \tag{9}$$

respectively. In equation (8), Da_s the dimensionless surface Damköhler number

$$Da_s \equiv \frac{k_s y_m}{D}. \tag{10}$$

Equation (6) with boundary conditions (8) and (9) form the dimensionless equation set for the blanket growth problem. Thus, there are only two parameters for this system, i.e., Da_b and Da_s.

3.3.1.3. Exact Solution

The dimensionless equations just derived can be further simplified by a separation of variables of the form

$$\hat{C}(\hat{y},\hat{t}) = \tilde{C}(\hat{y},\hat{t}) e^{-Da_b \hat{t}}. \tag{11}$$

Substituting the trial solution of equation (11) into equations (6), (8), and (9) yields

$$\frac{\partial \tilde{C}}{\partial \hat{t}} = \frac{\partial^2 \tilde{C}}{\partial \hat{y}^2} \tag{12}$$

$$\frac{\partial \tilde{C}}{\partial \hat{y}} = Da_s \tilde{C} \tag{13}$$

$$\frac{\partial \tilde{C}}{\partial \hat{y}} = 0. \tag{14}$$

The new, transformed equation set (12) – (14) has only one parameter, i.e., Da_s. The dimensionless equation (12) with boundary conditions (13) and (14) is identical in form to a well-known problem in heat transfer, the heat conduction in a plane wall with convection, for which an exact, infinite-series solution exists[85,86]. The exact solution is

$$\widehat{C}(\hat{y},\hat{t}) = \sum_{n=1}^{\infty} \widetilde{C}_n \exp(-\zeta_n \hat{t}) \cos(\zeta_n [1-\hat{y}]), \tag{15}$$

where the coefficients $\widetilde{C}_n$ are given by

$$\widetilde{C}_n = \frac{4\sin(\zeta_n)}{2\zeta_n + \sin(2\zeta_n)}; \tag{16}$$

the discrete values (eigenvalues) ζ_n are the positive roots of the transcendental equation

$$\zeta_n \tan(\zeta_n) = Da_s \ . \tag{17}$$

The full solution $\widehat{C}(\hat{y},\hat{t})$ is found from equations (15) and (11).

The (dimensionless) growth rate $\hat{g}$ can be obtained at any time as

$$\hat{g}(\hat{t}) = Da_s \widehat{C}(\hat{y}=0,\hat{t}) \ . \tag{18}$$

The total (cumulative) amount of dimensionless growth is found by integrating (18) in time, i.e.,

$$\widehat{G}(\hat{t}) = \int_0^{\hat{t}} g(\hat{t}')d\hat{t}' \ . \tag{19}$$

After some work, it can be shown that the cumulative growth amount up to time $\hat{t}$ is

$$\widehat{G}(\hat{t}) = Da_s \sum_{n=1}^{\infty} \frac{\widetilde{C}_n \cos(\zeta_n)}{\zeta_n^2 + Da_b} \left[1 - \exp\left(-\left\{\zeta_n^2 + Da_b\right\}\hat{t}\right)\right]. \tag{20}$$

And, finally, the total amount of growth at the surface at long time, i.e., $\hat{t} \to \infty$, is

$$\widehat{G} = Da_s \sum_{n=1}^{\infty} \frac{\widetilde{C}_n \cos(\zeta_n)}{\zeta_n^2 + Da_b} \ . \tag{21}$$

In practice, the infinite-series expansion result of equation (21) is inconvenient to work with, requiring a short computer routine to evaluate. However, it does serve several useful purposes. The process of non-dimensionalizing the problem helped to identify the two unique physical parameters that control the system, i.e., Da_s and Da_b. Having an exact solution for the growth allowed an independent check of the full finite-volume numerical calculation, described in Sec. 3.3.2.

3.3.2. Patterned Growth

3.3.2.1. Governing Equations and Boundary Conditions

The selective growth experiment must be modeled in two dimensions. Portions of the surface are masked so that no growth can occur; others are unmasked, allowing crystal growth. A schematic diagram of the 2-D model is shown Figure 13. Since reactants are depleted in the exposed regions of the surface, but not in the masked regions, there is a lateral concentration gradient. The reactants above masked zones diffuse toward the exposed regions, thus increasing the

amount of growth in the window areas (relative to the amount that would grow when the surface is completely unpatterned, i.e., in blanket growth).

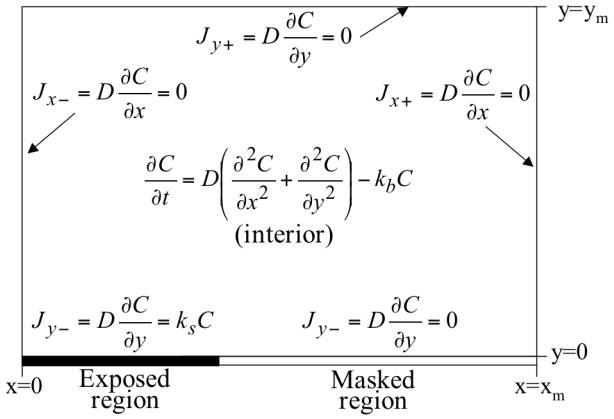

Figure 13. Schematic diagram for the 2-D model for selective-area growth.

Because of the symmetry of the experimental mask pattern we need to consider only half of repeated window / mask pattern, i.e., from the middle of one window region (defined as $x=0$) to the mid-point of the adjacent masked region (defined as $x=x_m$). By symmetry, there is no flux across the left or right boundaries.

The 2-D continuity equation describing the time-evolution of reactant concentration is

$$\frac{\partial C}{\partial t} = D\left(\frac{\partial^2 C}{\partial y^2} + \frac{\partial^2 C}{\partial x^2}\right) - k_b C\,. \tag{22}$$

The lower boundary condition ($y=0$) for the exposed regions (where growth occurs) is the same as before, i.e., equation (2)

$$J_{y-} = D\frac{\partial C}{\partial y} = k_s C\,. \tag{23}$$

A zero-flux boundary condition is applied for the masked regions (no growth)

$$J_{y-} = D\frac{\partial C}{\partial y} = 0\,. \tag{24}$$

A zero-flux boundary condition is applied at the top of the domain, as before

$$J_{y+} = D\frac{\partial C}{\partial y} = 0\,. \tag{25}$$

Zero-flux boundary conditions are imposed at the left and right boundaries, i.e.,

$$J_{x-} = D\frac{\partial C}{\partial x} = 0 \tag{26}$$

$$J_{x+} = D\frac{\partial C}{\partial x} = 0\,, \tag{27}$$

respectively.

3.3.2.2. Numerical Solution Method

A control volume (flux-balance) formulation of the governing equations was discretized to form a set of linear ordinary differential equations. The equations were integrated using the VODE software[87]. The 2-D reacting flow simulation was tested by comparing with the exact solution (for unpatterned growth) discussed in Section 3.3.1.

3.4. Results

3.4.2. Growth Experiments

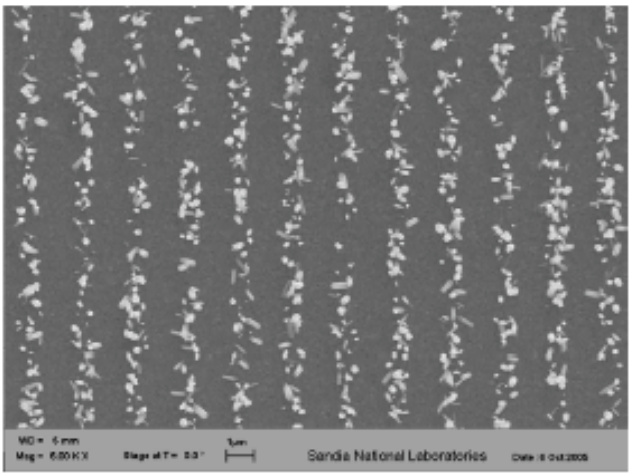

Figure 14. Plan view SEM image of ZnO nanorods grown using the 1:1 pattern.
i.e., 1 μm exposed lines separated by 1 μm regions of masked substrate.

The series of 12 different line patterns, varying in the dimensions of the exposed and masked zones, were studied. Plan view SEM images from the 1:1 pattern (1 μm exposed lines separated by 1 μm of mask) and 1:8 pattern (1 μm exposed lines separated by 8 μm of mask) are shown in Figure 14 and Figure 15, respectively. Good selectivity is achieved, with basically no ZnO growth in the masked regions.

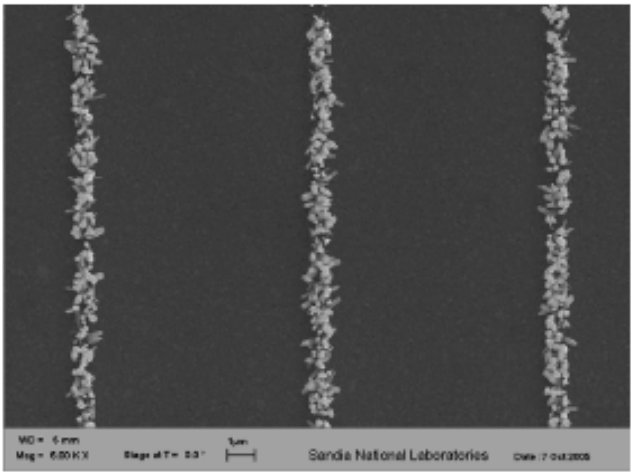

Figure 15. Plan view SEM image of ZnO nanorods grown using the 1:8 pattern.
i.e., 1 μm exposed lines separated by 8 μm regions of masked substrate.

It is readily seen that the amount of ZnO growth is greatly enhanced as the line separation is increased for a given window dimension, as reported earlier.[81] Also observed (but not represented here by an SEM image) was that for a fixed separation distance the density and height of the grown nanorods increased as the exposed zone was decreased.

To determine the amount of ZnO growth on a pattern's exposed region, we first measured the fractional area covered by the ZnO nanorods as obtained from analysis of the SEM images, e.g., Figure 14 and Figure 15. The areal fraction covered for each of the 12 patterns is given Table 1. In a representative region of unpatterned (blanket) growth, the fraction of surface covered by nanorods was determined to be 0.174.

The second step in the data analysis was to determine the average height of the nanorods for each pattern. This was done using AFM measurements of a sampling of individual nanorods in each pattern. The average nanorod heights for each pattern are also given in Table 1. The average height of nanorods grown in the unpatterned experiment was 0.55 μm. Thus the average amount of ZnO material growth in the unpatterned experiment is the product of the fraction of the surface covered times the average nanorod height, or 95.7 (in units of 10^{-3} μm^3) per square μm area of substrate.

For our selective growth experiments, the amount of ZnO growth as a function of the pattern repeat dimension (i.e., the sum of the exposed window and mask widths) is displayed in Figure 16. The growth amount plotted is the volume of ZnO grown (in units of 10^{-3} μm^3, as above) over the entire width of the pattern per micron length of the analyzed region. The different symbols in the figure represent different exposed line widths: 1 μm lines, circles; 2 μm lines, diamonds; 4 μm lines, triangles; 8 μm lines, squares. Also plotted in Figure 23 as the dotted line is the volume of ZnO that would grow over an unpatterned region 1 μm long and width given by the x-axis, for comparison.

Table 1. ZnO Nanorod Surface Coverage and Heights

Window (μm)	Mask (μm)	Fraction of surface covered	Average Height (nm)
1	1	0.140	667
1	2	0.118	649
1	4	0.072	635
1	4	0.072	612
1	8	0.056	678
1	16	0.048	692
1	32	0.036	735
2	4	0.071	596
2	16	0.056	635
4	4	0.084	559
4	16	0.056	623
8	4	0.123	579
8	16	0.078	638

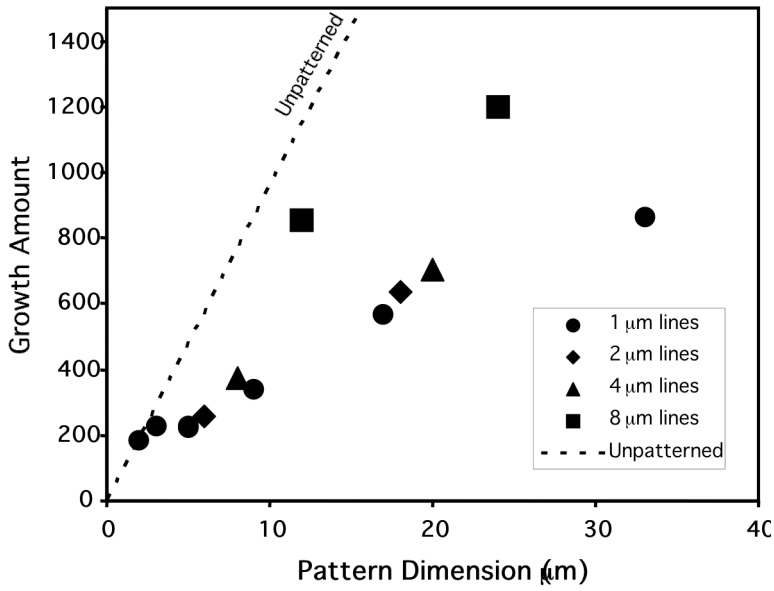

Figure 16. Volume of ZnO material grown in the exposed region as a function of the total repeat distance of the pattern.
(i.e., the sum of exposed region and masked region widths). See text for more details and explanation of the units.

For a given exposed line width, it is seen that the amount of ZnO grown increases roughly linearly with pattern width (or distance between the lines). Because a fraction of the substrate is masked, there is no growth in those regions. Thus, there is a large reservoir of reactant species

available for growth on the exposed areas. Reactant species travel within the bulk volume of the solution toward the growth zones by diffusive mass transport.

For a given lateral dimension, if the data symbol in Figure 23 approaches the dotted line (as is the case for the 1:1 and 1:2 patterns), that means that total amount of ZnO grown on the exposed lines approaches the amount that would have grown over the equivalent width (i.e., the width of the window plus mask) for unpatterned growth. That is, how close a given point lines to the equivalent unpatterned growth amount is a measure of how "efficient" this selective growth process is in diffusively transporting the reactant species to the exposed fraction of the surface. We define the growth efficiency as the amount of material grown in the exposed region divided by the amount of growth that would occur over an equivalent substrate area (mask plus growth region widths) if the surface were unpatterned. It is readily seen that the efficiency of the growth process drops off with increasing distance between the exposed regions. Thus, there is a length scale that governs aspects of the selective growth process.

It is also evident that total volume of material grown on the largest exposed windows (i.e., the 8 μm features, represented by the squares) is much greater than for the smallest lines. However, remember that those 8 μm lines have the largest "collection area" (they are 8 times wider than the 1 μm lines) for growth. So, although about twice as much material grows on the 8:4 feature (compared to the trend line of the other symbols), the *density* of growth (reflected in the fractional area covered and average nanorod height) is much *less* than on the narrower lines. This is another reflection of a pattern length scale affecting the process.

Close examination of the 1 μm line-width data also shows that the growth amount actually increases sub-linearly with distance between the lines. Thus, the selective growth efficiency has a length-scale associated with it.

In Figure 17 we plot the growth efficiency as defined above as a function of the fraction of the surface that is exposed for growth (e.g., the 1:4 pattern has 1 μm exposed for every 5 μm width of the surface, so its exposed fraction is 0.2). The exposed surface fraction is also referred to as the pattern "fill factor." The growth efficiency is highest for the smallest pattern dimensions, i.e., toward the right side of Figure 17. For a given exposed fraction, the process efficiency is greatest for the narrower lines. In the series of points for 1 μm lines (for which we have the most data), the efficiency drops precipitously as the fill factor gets very small. Of course this limit corresponds to very large distance between the lines, so the diffusive mass transport would have to be more and more facile to transport the reactants to the exposed lines for the efficiency to stay constant. Simple analysis can show that the efficiency must drop to zero as the fill-factor approaches zero. Similarly, the growth process efficiency must approach unity as the fill-factor approaches one (because, by definition, fill factor of one would correspond to an unpatterned surface).

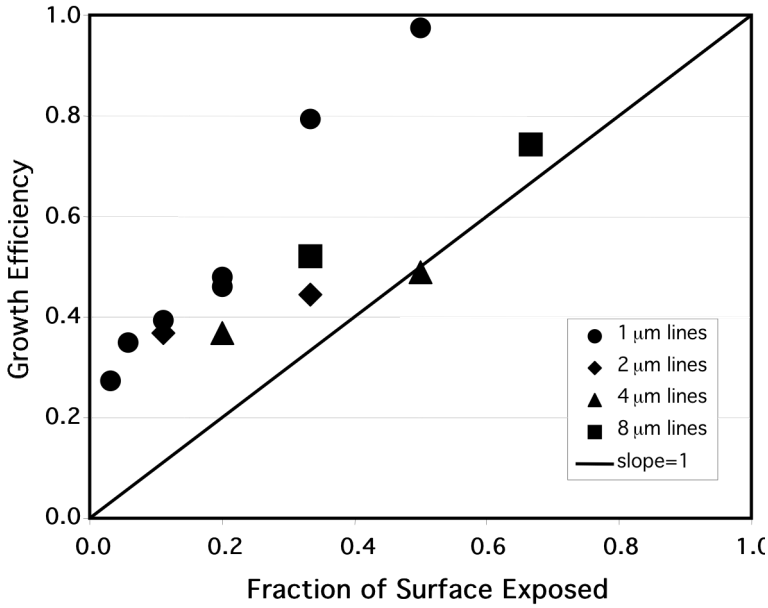

Figure 17. Selective growth efficiency (defined in the text) as a function of the fraction of the surface that is unmasked (i.e., exposed for growth).

3.4.2. Model of the Selective Growth Process

The selective growth process was simulated using the numerical model described in Section 3.2. There are three physical parameters in the model, i.e., the diffusion coefficient D, the surface rate constant k_s, and the rate constant for parasitic reactions in the solution bulk k_b. Diffusion constants for species in solution are typically on the order of 10^{-5} cm^2/s, and for simplicity D was fixed at that value. A simple variation of the other two parameters was performed in order to see if the general trends and experimental observations could be described by our 2-D reaction / transport model. Quantitative agreement between the model and experiment was not expected (or achieved). A more exact match to experiment would require a much more detailed treatment of the chemical reaction mechanism (and kinetics) both in the solution volume and at the surface. A reasonable fit to the experimental trends was achieved with parameter values k_s=5 cm/s and k_b=30 / s.

The ZnO growth amounts (in the same units as used earlier for Figure 23) calculated by the model as a function of pattern width (exposed region plus masked region widths) are displayed in Figure 18. Also plotted as the dashed line in Figure 25 is the growth amount that would occur for unpatterned growth (from experiment). The model reproduces most of the experimental trends that were seen in Figure 16. The total amount of material grown approaches the unpatterned amount at small pattern dimension. As the distance between the exposed lines is increased, the growth amount becomes sub-linear. The saturation of growth amount with increasing pattern dimension calculated by the model is stronger than was seen experimentally. The calculated growth is greatest for the 8 μm lines, as seen experimentally. The calculated growth amounts are in reasonable semi-quantitative agreement with experiment, especially

considering the relative simplicity of the model. However, as mentioned above, the saturation of growth amount with increasing pattern width calculated by the model is too strong.

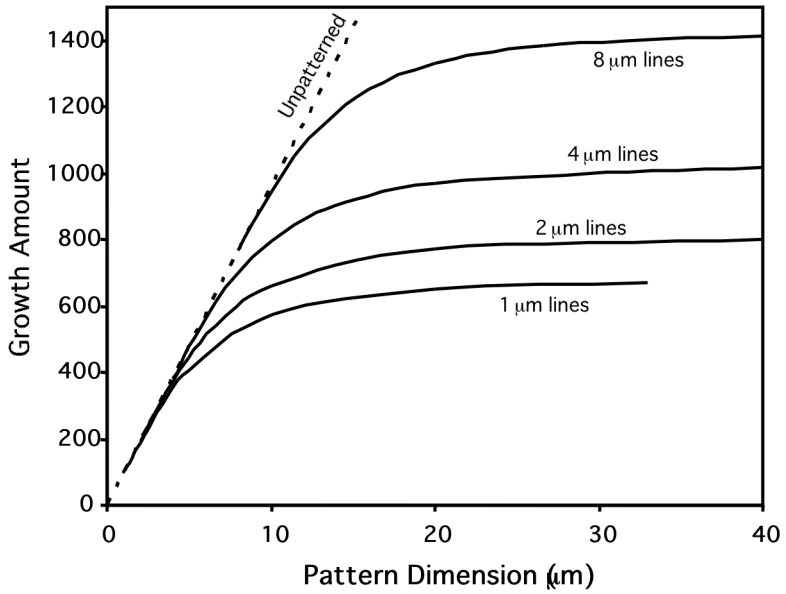

Figure 18. Model predictions of ZnO growth amount as a function of pattern dimension.

The calculated selective growth efficiency as a function of pattern fill factor is shown in Figure 26. The general trends observed in experiment are reproduced by the model. In fact, for the 1 μm lines (for which we have the most data), agreement between model is experiment is quite good. The decreasing growth efficiency with increasing exposed line width seen in the experiment is reproduced by the model.

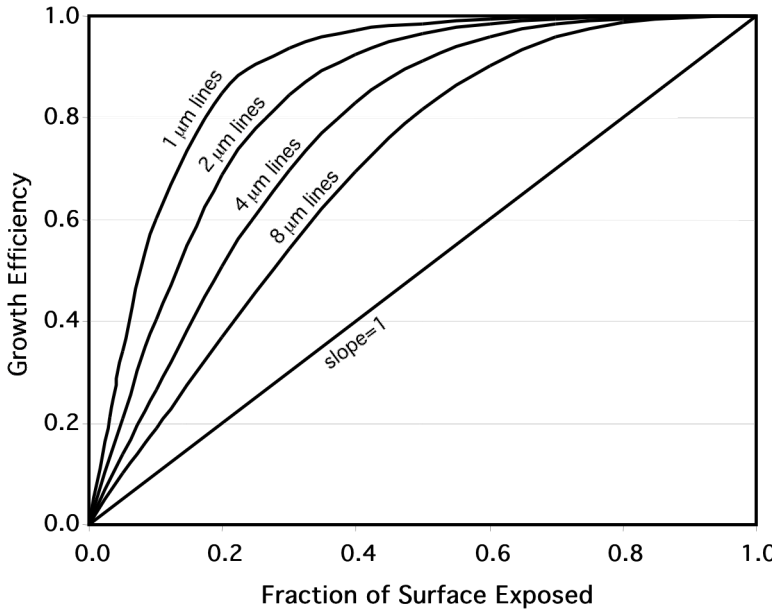

Figure 19. Model predictions of selective growth efficiency as a function of exposed surface fraction (fill-factor).

3.5. Conclusions

We have presented a quantitative study of the dependence of ZnO selective-area growth on pattern dimension. Selective growth is achieved by patterning a portion of the substrate with an organic template that inhibits growth. The density of ZnO nanorods increases as the distance between the exposed growth regions is made greater. By systematically varying the dimensions of the exposed and masked regions, the experiments showed that growth was partially controlled by a length scale associated with diffusive mass transport within the reactant solution.

A 2-D model was developed which describes the selective growth at the exposed surface regions, the competing loss of reactant material due to parasitic chemistry in the solution bulk, and diffusive mass transport to the growth surface. The simple model provides a good qualitative and semi-quantitative explanation of the experimental observations.

4. LUMINESCENT PROPERTIES OF SOLUTION-GROWN ZINC OXIDE NANORODS

The optical properties of solution-grown ZnO nanorods were investigated using photoluminescence and cathodoluminescence. The as-grown nanorods displayed a broad yellow-orange sub-bandgap luminescence and a small near-bandgap emission peak. The sub-bandgap luminescence can only be observed when exciting above bandgap. Scanning cathodoluminescence experiments showed that the width of the sub-bandgap luminescence is not due to an ensemble effect. Upon reduction, the sub-bandgap luminescence disappeared and the near-bandgap emission increased. Comparing to ZnO powders that are stoichiometric and oxygen deficient, we conclude that the yellow-orange sub-bandgap luminescence most likely arises from *bulk* defects that are associated with excess oxygen.

4.1. Introduction

The optical properties of solution-grown ZnO nanorods were investigated using photoluminescence and cathodoluminescence. The as-grown nanorods displayed a broad yellow-orange sub-bandgap luminescence and a small near-bandgap emission peak. The sub-bandgap luminescence can only be observed when exciting above bandgap. Scanning cathodoluminescence experiments showed that the width of the sub-bandgap luminescence is not due to an ensemble effect. Upon reduction, the sub-bandgap luminescence disappeared and the near-bandgap emission increased. Comparing to ZnO powders that are stoichiometric and oxygen deficient, we conclude that the yellow-orange sub-bandgap luminescence most likely arises from *bulk* defects that are associated with excess oxygen.

4.2. Experimental Section

The ZnO nanorods were grown from aqueous solutions of 20 mM zinc nitrate ($Zn(NO_3)_2$) and 20 mM hexamethylenetetramine ($(CH_2)_6N_4$) at 60 °C for 3 hours. The substrates were electron beam deposited Ag films on Si wafers. The nanorods are typically 100-200 nm in diameter and 500 nm tall. Smaller diameter rods (30-50 nm) can be made at higher growth temperature (92.5°C). Ag films were used as the substrate for ZnO growth because our previous work established that the majority of the ZnO nanorods are oriented with the <0001> axis perpendicular to the Ag substrate.[81] This study focused on samples with this preferential orientation and rod morphology. Annealing was performed in a tube furnace. For reference materials, Fisher reagent ZnO powder (oxidized form) was used as stoichiometric ZnO, and GTE 137 ZnO:Zn phosphor powder (reduced form) was used as oxygen-deficient ZnO.[88]

PL experiments were performed using Xe lamp excitation and pulsed and continuous wave (cw) UV laser light. Pulsed, UV excitation was provided by a laser system pumped by a 300 Hz, 1-watt, Nd:YLF laser, whose 1046-nm output was tripled (349 nm) or parametrically converted and quadrupled (232 nm). The average power of the laser at the UV wavelengths was 500 - 700 μW, and its pulse duration was 2 ns. Spectra were also taken using the (cw) 351 nm line from an argon ion laser. When using the Xe lamp, a monochromator and filter were used to isolate the excitation wavelength. PL emission was detected using a 0.6-m spectrograph and a liquid-

nitrogen-cooled, charge-coupled-device (CCD) detector. PL spectra have been corrected for the instrumental response over the wavelength ranges displayed. When comparing results taken at different excitation wavelengths, the intensities have been normalized by the lamp intensity at each wavelength. PL persistence was recorded using a photomultiplier tube (PMT) and a 500 MHz digital storage oscilloscope. The response of the instrumentation used to record persistence is limited by the rise time (9 ns) of the PMT. Scanning CL was employed to obtain high spatial resolution. The experiment was performed using a JEOL 845A scanning electron microscope equipped with an optical fiber mounted on a feedthrough for collecting light emission from the sample. In the imaging mode, the light was detected using a PMT; in the spectroscopy mode, the light was detected using a spectrograph and a CCD detector, as in PL. The experiments were done using an electron beam with 20 kV beam voltage and 0.5 – 5 nA beam current. All measurements were done at room temperature.

4.3. Results and Discussions

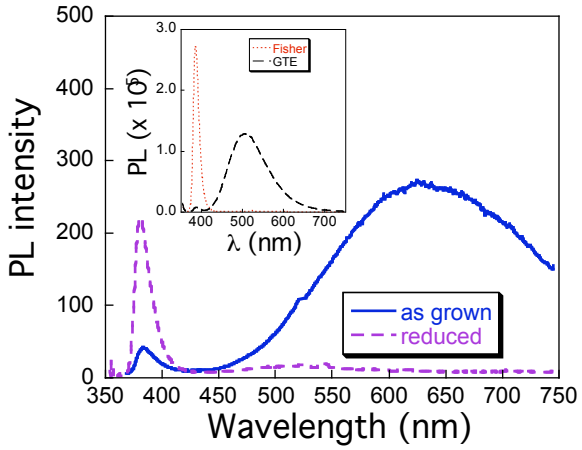

Figure 20. Photoluminescence (PL) intensity vs. emission wavelength.
For ensembles of ZnO nanorods as grown (blue solid line) and after the rods have been annealed in forming gas for 2 hours at 450°C (magenta dashed line). The inset shows the PL spectra for stoichiometric ZnO powder (Fisher, red dotted line) and ZnO:Zn powder (GTE, black dashed line). The excitation source was the tripled Nd:YLF pulsed laser at 349 nm.

Figure 20 shows the PL spectra for ZnO nanorods as grown and after annealing in forming gas (3% H_2 and 97% N_2). Data shown in the figure were taken using 349 nm excitation from the tripled Nd:YLF laser. Results obtained with the argon laser and Xe lamp excitation are similar. For as-grown rods, most of the spectral weight is in the sub-bandgap, centered around 625 nm. The center wavelength of the sub-bandgap luminescence can vary from 600 to 650 nm for different samples. But we did not observe emission shorter than 600 nm for as-grown nanorods. Recently, it has been reported that the sub-bandgap emission in ZnO depends on the morphology of the nanostructures.[89] The near bandgap emission (NBE) occurs at 384 nm and is much smaller compared to the defect luminescence. Under a fluorescence microscope with broad-band, near-UV excitation, the rods appear yellow-orange. Previous studies on ZnO mostly reported green sub-gap luminescence (peak near ~ 520 nm), which has been attributed to defects associated with

oxygen deficiency.[88] In the inset, the PL spectra for stoichiometric (Fisher) and oxygen-deficient ZnO:Zn (GTE phosphor) powders are shown. The visible emission from solution-grown ZnO nanorods is significantly red-shifted relative to that of oxygen-deficient ZnO powders and, therefore, most likely does not have the same origin. Longer wavelength sub-gap emission has been reported in a few papers.[55,89,90,91,92] We note that none of the ZnO samples that exhibit yellow-orange luminescence were made by vapor deposition. Vapor deposition produced samples that show either no sub-gap emission or green luminescence. Liu et. al. showed that annealing in moist air can change the luminescence from green to yellow.[91] We have found that annealing the nanorods in a reducing atmosphere (forming gas) at 450 °C for 30 min to 2 hours can eliminate the yellow-orange luminescence and enhance the NBE UV emission (Figure 20). H_2 is critical in this process; nanorods that are annealed in air or pure N_2 at the same temperature for the same amount of time show at most a 50% reduction in defect luminescence intensity but no significant enhancement in the UV emission. This result is consistent with previous suggestion that yellow-orange luminescence in ZnO is associated with excess oxygen, perhaps due to point defects such as oxygen interstitials.[90,91] Annealing in a reducing atmosphere could eliminate these defects and produce more stoichiometric rods. However, it should be noted that H_2 anneal can also introduce shallow donor states,[93] resulting in increased electron density and shifting of the Fermi level position, which in turn can change the occupation of deep levels and affect the branching ratio between exciton and defect recombination.

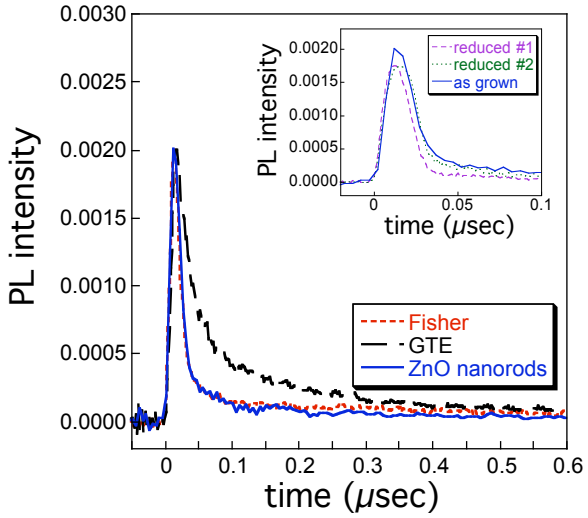

Figure 21. Persistence of deep emission intensity.
For as-grown ZnO nanorods (blue solid line), compared with stoichiometric (Fisher, red dotted line) and ZnO:Zn powders (GTE, black dashed line). The PL intensity was monitored at 620 and 530 nm for the ZnO nanorods and powders, respectively. The inset depicts the insensitivity of PL persistence with respect to annealing for nanorods (magenta dashed line and green dotted line).

Figure 21 compares the sub-bandgap emission persistence of the as grown ZnO nanorods with those of stoichiometric (Fisher) and oxygen-deficient ZnO:Zn (GTE) powders. It is evident that the PL of the oxygen-deficient ZnO has much slower relaxation dynamics, while that of the ZnO nanorods behaves similarly to the stoichiometric ZnO. The inset shows that the reducing

procedures we used did not have a strong effect on the PL persistence. These results further support our assertion that the defects associated with the yellow-orange luminescence in the solution-grown ZnO nanorods are different from those responsible for green luminescence in oxygen-deficient ZnO.

The width of the yellow-orange defect emission is quite broad, ~ 0.7 eV. Since the PL spectra are collected from an ensemble of ZnO nanorods, the spectral width of the deep emission could be the result of inhomogeneous broadening, i.e. different rods emitting at different wavelengths. To invesitigate this possibility, we employed CL imaging and spectroscopy. Figure 22 shows SEM and CL images of (a) a single ZnO nanorod and (b) a cluster of rods created by patterned growth.[81] We found that all the ZnO nanorods investigated are luminescent, with CL intensity varying by less than a factor of two for nanorods with diameters ranging from 100 to 400 nm. Figure 22(c) depicts the PL and CL spectra taken on an ensemble of nanorods; they are identical in the peak position and width of the defect luminescence. Furthermore, CL spectra of the deep emission for individual rods and for an ensemble have similar peak width and position (varying by ± 5 nm). Hence, the width of the yellow-orange defect luminescence is not caused by inhomogeneities among different rods, rather it is due to defect environments being inhomogeneous within a single nanorod. We note that no clear UV peak was observed in the CL spectra of individual rods.

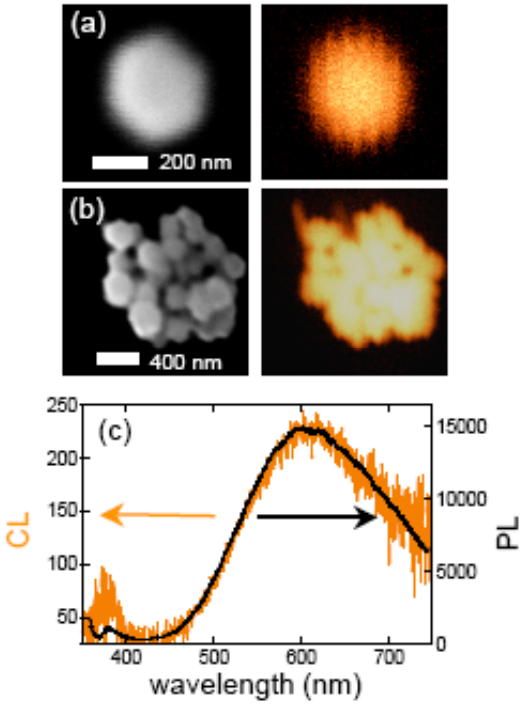

Figure 22. SEM (left) and CL (right) images of ZnO nanorods.
(a) an individual and (b) a cluster of ZnO nanorods. (c) CL (orange) and PL (black) spectra of an ensemble of as-grown ZnO nanorods. CL was taken at 20 kV and 5 nA beam current. PL excitation source was a continuous wave Ar laser at 351 nm.

We also found that the position and width of the yellow-orange emission do not depend on excitation wavelength from 270 to 380 nm (Figure 23 inset), and no sub-bandgap emission could be observed if excited below bandgap. Figure 23 shows the dependence of integrated PL intensity for the NBE (372-401 nm) and defect (500-745 nm) emission on excitation wavelength. Both peaks are most intense when excited at 355-360 nm. However, the two excitation curves do not have the same shape; the UV intensity increases much more strongly as a function of excitation wavelength. These results suggest that excitons are not directly involved in the defect emission process; instead, there exist efficient pathways to defect luminescence when an electron-hole pair is generated from absorbing light with above bandgap energy in ZnO nanorods.

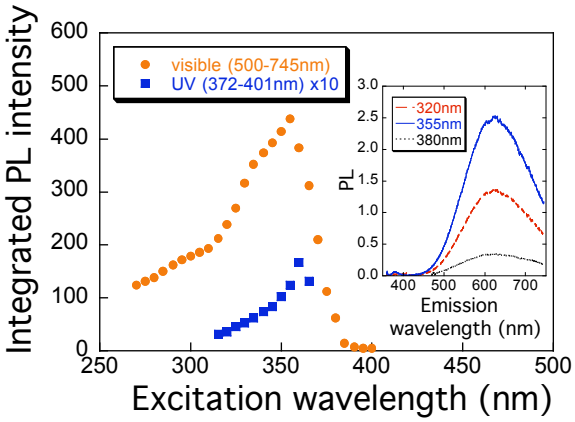

Figure 23. Integrated PL intensity vs. excitation wavelength.
Orange circles represent visible band (500-745 nm), and blue squares represent near bandgap UV emission (372-401 nm). The UV emission intensity was multiplied by 10. The UV emission cannot be measured past 365 nm due to the interference from the excitation light. Inset: The PL spectra for excitation wavelengths of 320 (red dashed line), 355 (blue solid line), and 380 nm (black dotted line). The excitation source was a Xe lamp and the results were normalized to lamp power at each wavelength.

Because of the large surface/volume ratio in nanostructures, surfaces are likely sites for defects. Recently, Shalish et. al. reported that the ratio of sub-bandgap emission at 550 nm to UV near-bandgap emission decreases as the diameter of ZnO nanowires increases from 50 to 250 nm, and concluded that surfaces are the origin of the defect luminescence in these ZnO nanowires grown by chemical vapor deposition.[94] When we performed PL measurements on samples with different diameter rods (30-50 nm vs. 100-200 nm), we found the ratios of yellow-orange defect luminescence to UV near band-gap luminescence are similar. Furthermore, we observed similar CL spectra for individual nanorods with diameters ranging from 100 to 400 nm. Combined with the finding that annealing in reducing atmosphere resulted in significant enhancement in exciton luminescence near bandgap, our results suggest that the defects responsible for the yellow-orange sub-bandgap emission most likely exist in the bulk of the solution-grown ZnO nanorods. Our conclusion agrees with the report by Li et. al. that surfactants on the surface of ZnO nanorods do not significantly affect the yellow luminescence, but do significantly reduce the green emission.[92] Hence, the defects associated with the yellow-orange luminescence would not

likely be surface deposits of zinc hydroxyls or organic molecules from the growth solution. The identification of specific defects associated with the yellow-orange luminescence is the subject of on-going research.

4.4. Summary

In summary, we have performed PL and PLE spectroscopy, PL persistence, scanning CL spectroscopy and imaging to probe the luminescent properties of solution-grown ZnO nanorods. As-grown nanorods display a strong yellow-orange sub-bandgap emission that is different from the more widely known green emission in oxygen deficient ZnO. Annealing and size studies suggest that the yellow-orange luminescence is most likely caused by *bulk* defects associated with excess oxygen. Scanning CL studies showed that this deep luminescence is similar for individual nanorods as for an ensemble of nanorods, suggesting a variety of defect environments. This deep emission relaxation pathway can be reached only through above-bandgap excitation and competes effectively against exciton emission.

5. ADDITIVE PATTERNING OF CONDUCTORS AND SUPERCONUDCTORS BY SOLUTION STAMPING NANOLITHOGRAPHY (SSNL)

Thin films of functional oxides, including ferro- and piezoelectrics, superconductors, and transparent conductors, are critical components for applications such as solar cells, energy storage, energy transport, and microelectromechanical systems. Conventionally, to pattern such oxide films, a thin film is blanket deposited on a substrate, followed by photolithography or electron-beam lithography patterning of an appropriate resist, and transfer of the resist pattern into the oxide film by chemical or physical etching. This lengthy process exposes the oxide materials to harsh chemicals and radiation, potentially inducing changes in chemical stoichiometry, defect content, and electronic properties. Furthermore, edge damage may arise from the subtractive etching processes, resulting in material inhomogeneity, which may be an acute issue for nanostructures. Here we introduce an additive approach, solution stamping nano-lithography (SSNL), in which printed metal organic inks are either oxidized to form functional oxides, or reduced to form metals. We demonstrate the technique by directly printing patterns of polycrystalline metallic Cu and epitaxial superconducting $YBa_2Cu_3O_{7-\delta}$ (YBCO) precursors. The structural and electrical properties of the converted film patterns illustrate the viability of this process. SSNL simplifies the feature-defining process and bypasses etching steps that can damage materials. This conformal printing approach can be extended to fabricating electrical circuits on unconventional curved or flexible substrates, such as plastics and textiles. Active "electronic paper" flexible displays and integrated sensors and tags on arbitrary surfaces for tracking and force protection are two areas for which this technique could have great impact.

5.1. Introduction

Chemical solution deposition (CSD) is a method capable of depositing high quality films of functional materials at a lower cost than vapor phase deposition.[95] The method enables low temperature processing, excellent stoichiometry control, and low cost, high throughput epitaxial film growth.[96] Previously, research groups have explored soft lithography techniques to create ceramic structures from sol-gel precursors, including micromolding in capillaries (MIMIC)[97] and micro-transfer molding, (μTM).[98] In addition, organic monolayers have been printed on surfaces via microcontact printing (μCP) to pattern subsequently-deposited sol-gel films without lithography or etching.[99] In this method, when the sol gel precursor solution is spun onto such a chemically patterned surface, the sol-gel solution only adheres to the portions of the substrate that were not functionalized with the hydrophobic monolayer. Thus, the organic template creates a negative "mask" for depositing inorganic materials. Later a removal process is needed to clean off the organic layer. Such an organosilane or thiol monolayer mask, however, can lead to film contamination and unreliable material patterning. At the nanometer scale, dip pen nanolithography (DPN) has been successfully demonstrated in depositing sol gel precursor patterns that are subsequently converted to inorganic materials.[100] However, DPN is a serial and time-consuming process. In this Communication, we describe an additive method to print sol-gel patterns, termed solution stamping nanolithography (SSNL). By stamping the precursor solution directly and selectively only on the regions in which the inorganic materials are desired, the rest of the surface remains pristine, and no negative mask is required. This is beneficial for cases in

which a second material will be subsequently grown in the uncoated regions. Furthermore, this is a parallel process in which patterns over large areas can be generated at once.

In SSNL, a polydimethylsiloxane (PDMS) elastomeric stamp containing relief patterns is first "inked" with a precursor solution of inorganic (functional oxide or ceramic) materials, and then placed on a substrate of choice to transfer this "ink" from the stamp to the substrate. Due to the flexible mechanical properties of the elastomeric material, the stamp forms a conformal contact with the surface, and ink transfer only occurs at locations where the stamp contacts the surface. Hence, the resulting patterns on the substrate mirror the stamp relief structures. The stamped precursor patterns are then processed following standard CSD procedures to convert them to the final composition of the desired inorganic material. If a lattice-matched substrate is used, the patterned thin films may be grown epitaxially on the underlying substrate.

5.2. Experimental Section

Two methods of inking the PDMS stamps were found to be effective. In the "spin-on" approach, a drop of sol-gel precursor is placed directly on the PDMS stamp and spun dry (Figure 24(a)). In the "pick-up" approach, an "ink pad" is created by spinning the solution on a clean Si wafer first; a clean PDMS stamp is then placed on the ink pad to pick up the sol gel precursor (Figure 24 (b)). The primary difference between the two methods is that there is no ink in the recessed regions of the stamp in the pick-up method. However, a thicker film could generally be deposited using the spin-on approach. Depending on the precursor solution, stamp feature size, and thickness required, the method that gives the best result was chosen. It should be noted the inks used in this work display very low volatility compared to traditional sol-gel precursors; thus the ink remains liquid instead of forming unprintable, rigid films on the stamp.

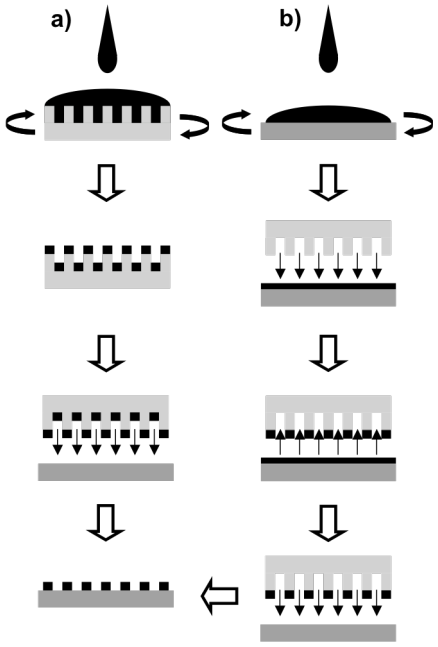

Figure 24. Schematics of solution stamping nano-lithography (SSNL).

Two methods to ink stamps: (a) spin-on and (b) pick-up.

Following deposition, the ink is "set" by heating the sample on a hot plate to remove leftover solvent. The setting step is important for two reasons: (i) to stop movement of deposited ink on the sample (e.g., dewetting), and (ii) to prevent uncontrolled crystallization or chemical segregation. The sample is then pyrolyzed in an oven to decompose the organic component in the sol gel precursor. After pyrolysis, YBCO patterns were subsequently crystallized.[101] To prepare Cu patterns, the precursor patterns were pyrolyzed to form CuO, which is then reduced to Cu metal.

5.3. Results

Figure 25 shows various precursor patterns created using SSNL: (a) 70μm-wide lines of as-stamped YBCO, (b) 1 μm Cu dots, and (c, d) 3μm-wide Cu lines on an 8-μm pitch. The stamping may be performed multiple times; Figure 25(e) depicts crossed lines by printing a line sample twice, the second time perpendicular to the first. We found that the best results were achieved when the first set of patterns were set before the second stamping. Figure 25(f) illustrates printing on a curved surface, a glass microcapillary with 1 mm diameter. In this image, the printed lines have been converted to Cu.

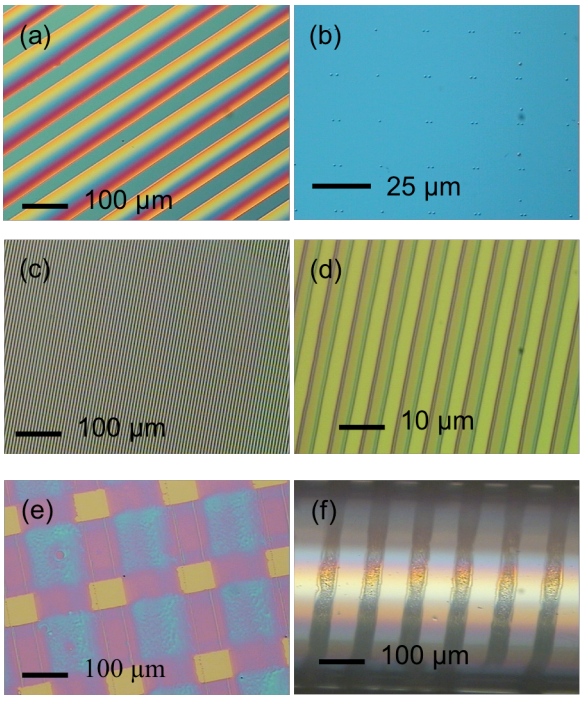

Figure 25. Gallery of optical micrographs of patterns produced using SSNL.
(a) As-printed 70μm-wide lines of YBCO precursor. Cu precursor patterns after setting: (b) 1 μm dots, (c) and (d) 3μm Cu lines on a 8-μm pitch. (e) Crossed Cu precursor lines by printing a line sample twice, the second time perpendicular to the first. The first set of lines were set at 200°C for 5s and cooled for at lease 3 min. before the second stamping. (f) Fully converted printed Cu lines on a curved glass microcapillary of 1 mm diameter.

The electrical properties of the Cu patterns made from SSNL were shown in Figure 26. Meandering lines of 200μm-wide lines (0.25μm thick) over 1 mm in length were printed on insulating SiO_x substrate (lower right inset of Figure 26). The current vs. voltage and resistance vs. length (upper left inset) curves are both linear (Figure 26). The resistivity of these SSNL Cu lines was measured to be 7.4-8.1 μΩ-cm, approximately five times the bulk Cu resistivity value of 1.7 μΩ-cm.[102] Since SSNL creates polycrystalline materials, internal porosity or cross-section nonuniformity could contribute to this higher measured resistivity value. Direct printing of Cu lines has been demonstrated via nanotransfer printing (nTP).[103] Compared with nTP, SSNL does not need an organic binder at the interface and therefore can be applied to a wide variety of substrates; in addition, it is possible to generate thicker films using SSNL.

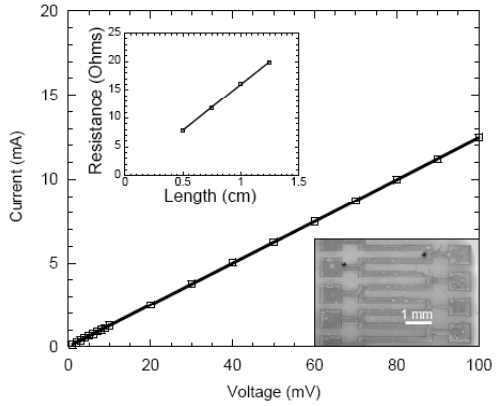

Figure 26. Electrical characterization of 200μm wide Cu lines made using SSNL. Linear relationship was observed for current versus voltage and resistance versus length (upper left inset). The lower right inset is a scanning electron microscopy image of the printed Cu patterns used in the electrical measurement.

Figure 27 illustrates the application of SSNL to create nanostructures. Figure 27(a) is an atomic force microscopy image of Cu dots of ~ 600nm in diameter made by direct printing of highly wetting inks, as described before. In addition to making stamps with smaller feature size, a molded dewetting method,[104] in which the stamp is held in place and the dilute ink recedes from the center of the contact regions to form beads outlining the edges, can be exploited to create nanostructures. Figure 27(b) shows that 250-300 nm diameter dots outlining the edges of 3-μm lines were generated by the this approach. Further extension of this approach to create sub-100 nm size features can be achieved through optimizing the concentration of active components in the precursor solution and the interaction between the solution and the surfaces of the stamp and substrate.

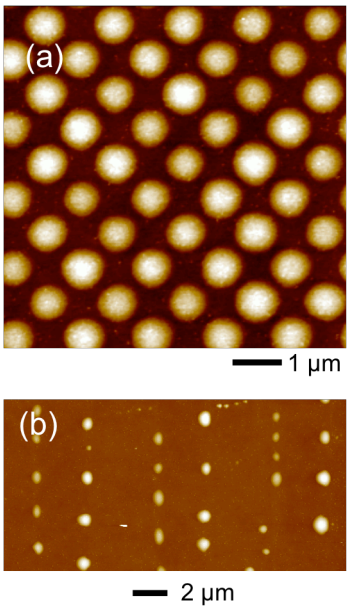

Figure 27. Atomic force microscopy images of nanostructures printed via SSNL.
(a) 650 nm directly printed Cu dots, and (b) Cu dots as small as 250 nm, formed by molded dewetting of dilute precursor.

The SSNL process has also been applied to create patterns of YBCO, a high-temperature superconductor, for which a facile method of producing patterned films would be advantageous for superconducting wire applications.[105] Both large area (~100µm) line patterns and micron-size YBCO patterns have been printed. X-ray diffraction (XRD) results on the YBCO (a = 3.82Å) patterns on (100) $LaAlO_3$ (a = 3.77Å) substrates indicate epitaxial YBCO (001) growth of the printed inks on the lattice-matched substrates (Figure 28(a)). The onset of the superconducting transition of these films was measured to be 85 K (Figure 28(b)), and the critical current density at liquid nitrogen temperature (77 K) was 280,000 A/cm^2, comparable to blanket deposited films spin coated from the same precursor. Films with current densities in excess of 1 MA/cm^2 would be expected with some optimization; a minority phase of Y_2BaCuO_5 (YBCO 211) appears in the XRD pattern, indicative of copper deficiency. Thus, SSNL is expected to be capable of patterning other epitaxial oxide films in addition to YBCO in a simple, one-step process.

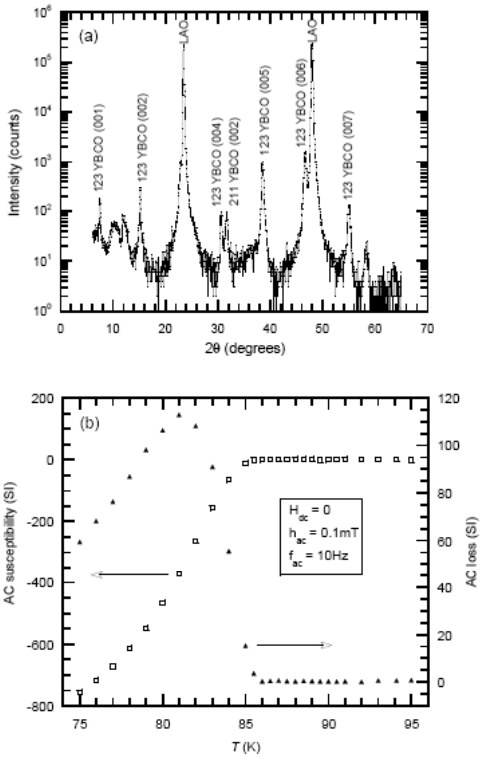

Figure 28. Characterization of printed YBCO lines made using SSNL.
(a) X-ray diffraction: $YBa_2Cu_3O_{7-x}$, Y_2BaCuO_5, and $LaAlO_3$ peaks are denoted 123 YBCO, 211 YBCO, and LAO, respectively. (b) Meissner magnetization measurements of SSNL YBCO, indicating the onset of superconducting transition at 85K.

5.4. Summary

In summary, an additive solution stamping process to directly create patterned conductors and superconductors has been developed through the use of low-volatility precursors. The technique is simple and can be used to make a variety of materials with a wide range of sizes and thicknesses. Similar to other soft lithography techniques, SSNL may be used to print patterned functional oxides on flexible or curved substrates without the need for subsequent etching, and may be a useful method for direct functional materials integration.

6. REFERENCES

[1] B. C. Bunker, P. C. Rieke, B. J. Tarasevich, A. A. Campbell, G. E. Fryxell, G. L. Graff, L. Song, J. Liu, J. W. Virden, *Science* **1994**, *264*, 48.

[2] Aizenberg, J.; Black, A. J.; Whitesides, G. M. *Nature* **1999**, *398*, 495.

[3] Meldrum, F. C.; Flath, J.; Knoll, W. *Thin Solid Films* **1999**, *348*, 188.

[4] Chen, C. C.; Lin, J. J. *Adv. Mater.* **2001**, *13*, 136.

[5] Huang, M. H. et al. *Science* **2001**, *292*, 1897.

[6] Pan, Z. W.; Dai, Z. R.; Wang, Z. L. *Science* **2001**, *291*, 1947.

[7] Lao, J. Y.; Wen, J. G.; Ren, Z. F. *Nano Lett.* **2002**, *2*, 1287.

[8] Muthukumar, S., et al. *IEEE Trans. Nanotechnol.* **2003**, *2*, 50.

[9] Li, W. J.; Shi, E. W.; Zhong, W. Z.; Yin, Z. W. *J. Cryst. Growth* **1999**, *203*, 186.

[10] Vayssieres, L.; Keis, K.; Lindquist, S. E.; Hagfeldt, A. *J. Phys. Chem.*, B **2001**, *105*, 3350.

[11] Tian, Z. R.; Voigt, J. A.; Liu, J.; Mckenzie, B.; Mcdermott, M. J. *J. Am. Chem. Soc.* **2002**, *124*, 12954.

[12] Tian, Z. R., et al. *Nat. Mater.* **2003**, *2*, 821.

[13] Han, Y. J.; Aizenberg, J. *J. Am. Chem. Soc.* **2003**, *125*, 4032.

[14] Xia, Y.; Whitesides, G. M. *Angew. Chem. Int. Edn. Eng.* **1998**, *37*, 550.

[15] Travaille, A. M. et al. *Adv. Mater.* **2002**, *14*, 492.

[16] Onuma, K. et al. *J. Phys. Chem.*, B **2000**, *104*, 11950.

[17] Baes, C. F.; Mesmer, R. E. *The hydrolysis of cations*, reprinted ed,; John Wiley and Sons, Inc.: New York, 1986.

[18] Tada, H. *J. Am. Chem.* Soc. **1960**, *82*, 255.

[19] Narkulov, A. N.; Yunusov, D. Kh.; Kim-Lin-Zu, V. A. *Zhurnal Prikladnoi Khimii,* **1987**, *80*, 882.

[20] The pH value for the onset of ionization of the $HSC_{10}H_{20}COOH$ monolayer is ~ 6, which is 3 units higher than PK_a value for carboxylic acids in aqueous solution. See Bain, C. D.; Whitesides, G. M. *Langmuir*, **1989**, *5*, 1370.

[21] R. Wagner, W. Ellis, *Appl. Phys. Lett.* **1964**, *4*, 89.

[22] W. Z. Li, S. S. Xie, L. X. Qian, B. H. Chang, B. S. Zou, W. Y. Zhou, R. A. Zhao, G. Wang, *Science* **1996**, *274*, 1701.

[23] Z. F. Ren, Z. P. Huang, J. W. Xu, J. H. Wang, P. Bush, M. P. Siegel, P. N. Provencio, *Science* **1998**, *282*, 1105.

[24] M. Huang, S. Mao, H. Feick, H. Yan, Y. Wu, H. Kind, E. Weber, R. Russo, P. Yang, *Science* **2001**, *292*, 1897.

[25] M. H. Huang, Y. Wu, H. Feick, N. Tran, E. Weber, P. Yang, *Adv. Mater.* **2001**, *13*, 113.

[26] D. P. Yu, Y. J. Xing, Q. L. Hang, H. F. Yang, J. Xu, Z. H. Xi, S. Q. Feng, *Physica E* **2001**, *9*, 305.

[27] L. C. Chen, S. W. Chang, C. S. Chang, C. Y. Wen, J.-J. Wu, Y. F. Chen, Y. S. Huang, K. H. Chen, *J. Phys. Chem. Solids* **2001**, *62*, 1567.

[28] T. Niesen, M. De Guire, *J. Electroceramics* **2001**, *6*, 169.

[29] L. Addadi, J. Moradian, E. Shay, N. G. Maroudas, S. Weiner, *Proc. Natl. Acad. Sci. U. S. A.* **1987**, *87*, 2732.

[30] S. Weiner, *Crit. Rev. Biochem.* **1986**, *20*, 365.

[31] P. C. Rieke, B. D. Marsh, L. L. Wood, B. J. Tarasevich, J. Liu, L. Song, G. E. Fryxell, *Langmuir* **1994**, *11*, 318.

[32] B. J. Tarasevich, P. C. Rieke, J. Liu, *Chem. Mater.* **1996**, *8*, 292.
[33] L. Vayssieres, N. Beermann, S. E. Lindguist, A. Hagfeldt, *Chem. Mater.* **2001**, *13*, 233.
[34] L. Vayssieres, L. Rabenberg, A. Manthiram, *Nano Lett.* **2002**, *2*, 1393.
[35] L. Vayssieres, K. Keis, A. Hagfeldt, S.-E. Linquist, *Chem. Mater.* **2001**, *13*, 4395.
[36] L. Vayssieres, *Adv. Mater.* **2003**, *15*, 464.
[37] K. Govender, D. S. Boyle, P. B. Kenway, P. O'Brien, *J. Mater. Chem.* **2004**, *14*, 2575.
[38] W. Zhang, X. Wen, S. Yang, *Inorg. Chem.* **2003**, *42*, 5005.
[39] W. Zhang, X. Wen, S. Yang, Y. Berta, Z. L. Wang, *Adv. Mater.* **2003**, *15*, 822.
[40] L. Zhang, J. C. Yu, M. Mo, L. Wu, Q. Li, K. W. Kwong, *J. Am. Chem. Soc.* **2004**, *126*, 8116.
[41] H. Hou, Y. Xie, Q. Li, *Cryst. Growth Des.* **2005**, *5*, 201.
[42] Y. Li, Z. Wang, X.-d. Ma, X.-f. Qian, J. Yin, Z.-K. Zhu, *J. Solid State Chem.* **2004**, *177*, 4386.
[43] S. Peulon, D. Lincot, *J. Electrochem. Soc.* **1998**, *145*, 864.
[44] R. Konenkamp, K. Boedecker, M. C. Lux-Steiner, M. Poschenrieder, E. Zenia, C. Leavy-Clement, *Appl. Phys. Lett.* **2000**, *77*, 2575.
[45] M. Wong, A. Berenov, X. Qi, M. Kappers, Z. Barber, B. Illy, Z. Lockman, M. Ryan, J. MacManus-Driscoll, *Nanotechnology* **2003**, *14*, 968.
[46] M. Izaki, T. Omi, *Appl. Phys. Lett.* **1996**, *68*, 2439.
[47] B. Canava, D. Lincot, *J. Appl. Electrochem.* **2000**, *30*, 711.
[48] R. Liu, A. A. Vertegel, E. W. Bohannan, T. A. Sorenson, J. A. Switzer, *Chem. Mater.* **2001**, *13*, 508.
[49] R. Liu, F. Oba, E. W. Bohannan, F. Ernst, J. A. Switzer, *Chem. Mater.* **2003**, *15*, 4882.
[50] M. J. Siegfried, K.-S. Choi, *Adv. Mater.* **2004**, *16*, 1743.
[51] M. Maosong, J. C. Yu, L. Zhang, S.-K. A. Li, *Adv. Mater.* **2005**, *17*, 756.
[52] Z. Wang, X.-f. Qian, J. Yin, Z.-k. Zhu, *Langmuir* **2004**, *20*, 3441.
[53] X. Gao, X. Li, W. Yu, *J. Phys. Chem. B* **2005**, *109*, 1155.
[54] A. Jackson, J. Vincent, R. Turner, *Proc. R. Soc. London, B* **1988**, *234*, 415.
[55] L. E. Greene, M. Law, J. Goldberger, F. Kim, J. C. Johnson, Y. Zhang, R. J. Saykally, P. Yang, *Angew. Chem., Int. Ed.* **2003**, *42*, 3031.
[56] Z. Tian, J. Voigt, J. Liu, B. McKenzie, H. Xu, *J. Am. Chem. Soc.* **2003**, *125*, 12384.
[57] J. Choy, E. Jang, J. Won, J. Chung, D. Jang, Y. Kim, *Adv. Mater.* **2003**, *15*, 1911.
[58] J.-H. Choy, E.-S. Jang, J.-H. Won, J.-H. Chung, D.-J. Jang, Y.-W. Kim, *Appl. Phys. Lett.* **2004**, *84*, 287.
[59] S. Yamabi, H. Imai, *J. Mater. Chem.* **2002**, *12*, 3773.
[60] C.-H. Hung, W.-T. Whang, *Mater. Chem. Phys.* **2003**, *82*, 705.
[61] E. Wong, P. Searson, *Appl. Phys. Lett.* **1999**, *74*, 2939.
[62] Q. C. Li, V. Kumar, Y. Li, H. T. Zhang, T. J. Marks, R. P. H. Chang, *Chem. Mater.* **2005**, *17*, 1001.
[63] S.-C. Liou, C.-S. hsiao, S.-Y. Chen, *J. Cryst. Growth* **2005**, *274*, 438.
[64] H. Yu, Z. Zhang, M. Han, X. Hao, F. Zhu, *J. Am. Chem. Soc.* **2005**, *127*, 2378.
[65] R. B. Peterson, C. L. Fields, B. A. Gregg, *Langmuir* **2004**, *20*, 5114.
[66] D. S. Boyle, K. Govender, P. O'Brien, *Chem. Commun.* **2002**, *1*, 80.
[67] L. Liang, J. Liu, J. C. F. Windisch, G. J. Exarhos, Y. Lin, *Angew. Chem., Int. Ed.* **2002**, *41*, 3665.
[68] J. Liu, Y. Lin, L. Liang, J. A. Voigt, D. L. Huber, Z. R. Tian., E. Coker, B. Mckenzie, M. J. Mcdermott, *Chem. - Eur. J.* **2003**, *9*, 604.

[69] D. Zhou, E. Anoishkina, V. Desai, K. Casey, *Electrochem. Solid-State Lett.* **1998**, *1*, 133.
[70] S. Hirano, K. Masuya, M. Kuwabara, *J. Phys. Chem. B* **2004**, *108*, 4576.
[71] S. Hirano, K. Masuya, M. Kuwabara, *J. Phys. Chem. B* **2004**, *108*, 4576.
[72] K. A. Dick, K. Deppert, M. Larsson, T. Martensson, W. Seifert, L. Wallenberg, L. Samuelson, *Nat. Mater.* **2004**, *3*, 380.
[73] X. Gao, Z. Zheng, H. Zhu, G. Pan, J. Bao, F. Wu, D. Song, *Chem. Commun.* **2004**, *12*, 1428.
[74] H. Yang, H. Zeng, *J. Am. Chem. Soc.* **2005**, *127*, 270.
[75] B. Liu, H. Zeng, *Langmuir* **2004**, *20*, 4196.
[76] J. C. F. Baes, R. E. Mesmer, *The Hydrolysis of Cations*, John Wiley & Sons, New York **1976**.
[77] B. G. Wang, E. W. Shi, W. Z. Zhong, *Cryst. Res. Technol.* **1998**, *33*, 937.
[78] Y. Yan, M. M. Al-Jassim, M. Chisholm, L. Boatner, S. Pennycook, M. Oxley, *Phys. Rev. B: Condens. Matter* **2005**, *71*, 041309.
[79] J. Aizenberg, *J. Cryst. Growth* **2000**, *211*, 143.
[80] J. Aizenberg, *Adv. Mater.* **2004**, *16*, 1295.
[81] J. W. P. Hsu, Z. R. Tian, N. C. Simmons, C. M. Matzke, J. A. Voigt, and J. Liu, Nano Lett. **5**, 83 (2005)
[82] R. McBride, J. Kelly, D. McCormack, *J. Mater. Chem.* **2003**, *13*, 1196.
[83] Z. R. Tian, J. Liu, J. A. Voigt, B. Mckenzie, X. Huifang, *Angew. Chem., Int. Ed.* **2003**, *42*, 413.
[84] Hsu, J.W.P., Z.R. Tian, N.C. Simmons, C.M. Matzke, J.A. Voight, and J. Liu, Proc. SPIE, 5592, 158 (2004).
[85] Schneider, P.J., "Conduction Heat Transfer," Addison-Wesley, Reading, MA, 1955.
[86] Incropera, F.P., and D.P. DeWitt, "Fundamentals of Heat and Mass Transfer," 4th ed., John Wiley and Sons, 1996.
[87] Brown, P.N., G.D. Byrne, and A.C. Hindmarsh, SIAM J. Sci. Stat. Comp., 10, 1038 (1989).
[88] K. Vanheusden, W. L. Warren, C. H. Seager, D. R. Tallant, J. A. Voigt, and B. E. Gnade, J. Appl. Phys. **79**, 7983 (1996)
[89] W. M. Kwok, A. B. Djurisic, Y. H. Leung, W. K. Chan, and D. L. Phillips, Appl. Phys. Lett. 87, 223111 (2005)
[90] S. A. Studenikin, N. Golego, and M. Cocivera, J. Appl. Phys. **84**, 2287 (1998)
[91] M. Liu, A. H. Kitai, and P. Mascher, J. Lumin. **54**, 35 (1992)
[92] D. Li, Y. H. Leung, A. B. Djurisic, Z. T. Liu, M. H. Xie, S. L. Shi, S. J. Xu, and W. K. Chan, Appl. Phys. Lett. **85**, 1601 (2004)
[93] C. H. Seager and S. M. Myers, J. Appl. Phys. **94**, 2888 (2003)
[94] I. Shalish, H. Temkin, and V. Naryanamurti, Phys. Rev. B **69**, 245401 (2004)
[95] A. Sheth, H. Schmidt, V. Lasrado, *Appl. Supercon.* **1998**, *6*, 855.
[96] a) R. Schwartz, *Chem. Mater.* **1997,** *9*, 2325; b) F.F. Lange, *Science* **1996**, *273*, 903.
[97] a) E. Kim, Y. Xia, G. M. Whitesides, *J. Am. Chem. Soc.* **1996**, *118*, 5722; b) C. R. Martin, I. A. Aksay, *J. Phys. Chem. B* **2003**, *107*, 4261.
[98] a) X.-M. Zhao, Y. Xia, G. Whitesides, *Adv. Mater.* **1996**, *8*, 837; b) J. H. Kim, F.F. Lange, C.-I. Cheon, *J. Mater. Res.* **1999**, *14*, 1194.
[99] a) P. G. Clem, N. L. Jeon, R. G. Nuzzo, D. A. Payne, *J. Am. Ceram. Soc.* **1997**, *80*, 2821; b) N. L. Jeon, P. Clem, D. Y. Jung, W. Lin, G. S. Girolami, D. A. Payne, R. G. Nuzzo, *Adv. Mater.* **1997***, 9*, 891; c) N. L. Jeon, P. G. Clem, R. G. Nuzzo, D. A. Payne, *J. Mater. Res.* **1995**, *10*, 2996.

[100] a) M. Su, X. Liu, S.-Y. Li, V. P. Dravid, C. A. Mirkin, *J. Am. Chem. Soc.* **2002**, *124*, 1560; b) L. Fu, X. Liu, Y. Zhang, V. P. Dravid, C. A. Mirkin, *Nano Lett.* **2003**, *3*, 757.
[101] M. P. Siegal, J. T. Dawley, P. G. Clem, D. L. Overmyer, *Physica C* **2003**, *399*, 143.
[102] C. Kittel, *Introduction to Solid State Physics*, 7th ed., John Wiley & Sons, Inc., New York, **1996**, p.160.
[103] K. Felmet, Y.-L. Loo, and Y. Sun, *Appl. Phys. Lett.* **2004**, *85*, 3316.
[104] H.-L. Zhang, D. G. Bucknall, A. Dupius, *Nano Lett.* **2004**, *4*, 1513.
[105] N. Amemiya, S. Kasai, K. Yoda, Z.N. Jiang, G.A. Levin, P.N. Barnes, C.E Oberly, *Supercond. Sci. Technol.* **2004**, *17*, 1464.

DISTRIBUTION

2	MS9018	Central Technical Files	8944
2	MS0899	Technical Library	4536
1	MS0123	D. Chavez, LDRD Office	1011
1	MS0885	J. E. Johannes	1810
1	MS0887	D. B. Dimos	1800
1	MS1086	M. E. Coltrin	1126
1	MS1411	J. A. Voigt	1816
1	MS1411	D. R. Tallant	1822
1	MS1411	P. G. Clem	1824
1	MS1415	R. Q. Hwang	1110
1	MS1415	C. Gutierrez	1114
1	MS1415	N. A. Missert	1112
1	MS1427	J. M. Phillips	1100


Sandia National Laboratories